

The near-IR $M_{\text{bh}}-L$ and $M_{\text{bh}}-n$ relations

Marina Vika,^{1,2} Simon P. Driver,^{1,2} Ewan Cameron,³ Lee Kelvin,^{1,2} Aaron Robotham,^{1,2}

¹*Scottish Universities Physics Alliance (SUPA)*

²*School of Physics & Astronomy, University of St Andrews, North Haugh, St Andrews, Fife, KY16 9SS*

³*Department of Physics, Swiss Federal Institute of Technology(ETH-Zürich), CH-8093 Zürich, Switzerland*

Received XXXX; Accepted XXXX

ABSTRACT

We present near-IR surface photometry (2D-profiling) for a sample of 29 nearby galaxies for which super-massive black hole (SMBH) masses are constrained. The data is derived from the UKIDSS-LASS survey representing a significant improvement in image quality and depth over previous studies based on 2MASS data. We derive the spheroid luminosity and spheroid Sérsic index for each galaxy with GALFIT3 and use these data to construct SMBH mass -bulge luminosity ($M_{\text{bh}}-L$) and SMBH - Sérsic index ($M_{\text{bh}}-n$) relations. The best fit K-band relation for elliptical and disk galaxies is $\log(M_{\text{bh}}/M_{\odot}) = -0.36(\pm 0.03)(M_K + 18) + 6.17(\pm 0.16)$ with an intrinsic scatter of $0.4_{-0.06}^{+0.09}$ dex whilst for elliptical galaxies we find $\log(M_{\text{bh}}/M_{\odot}) = -0.42(\pm 0.06)(M_K + 22) + 7.5(\pm 0.15)$ with an intrinsic scatter of $0.31_{-0.047}^{+0.087}$ dex. Our revised $M_{\text{bh}}-L$ relation agrees closely with the previous near-IR constraint by Graham (2007). The lack of improvement in the intrinsic scatter in moving to higher quality near-IR data suggests that the SMBH relations are not currently limited by the quality of the imaging data but is either intrinsic or a result of uncertainty in the precise number of required components required in the profiling process. Contrary to expectation (see Graham & Driver 2007) a relation between SMBH mass and the Sérsic index was not found at near-IR wavelengths. This latter outcome is believed to be explained by the generic inconsistencies between 1D and 2D galaxy profiling which are currently under further investigation.

Key words: galaxies: bulges — galaxies: fundamental parameters — galaxies: photometry — galaxies: nuclei — galaxies: structure —

1 INTRODUCTION

The number of SMBH mass measurements (M_{bh}) from inactive galaxies in the local Universe have rapidly increased over the last 15 years (see Graham et al. 2010, hereafter GO10 for sample compilation). Kormendy & Richstone (1995) reviewed M_{bh} determinations for a sample of 8 local galaxies and introduced the SMBH mass (M_{bh}) - galaxy luminosity (L , or bulge luminosity in the case of disk galaxies) relation¹. Since this time, the $M_{\text{bh}}-L$ correlation has been investigated by a number of groups from optical to near-IR passbands (Magorrian et al. 1998; Kormendy & Gebhardt 2001; Marconi & Hunt 2003; Graham 2007; Gültekin et al. 2009).

Establishing an accurate $M_{\text{bh}}-L$ relation is beneficial for two reasons: firstly to understand the physical basis as

to why the relation exists and secondly to provide a means for predicting SMBH masses for large samples of galaxies (e.g. Graham et al. 2007; Vika et al. 2009). Furthermore Active Galactic Nuclei (AGN) are the antecedent of most local inactive galaxies, studying the $M_{\text{bh}}-L$ relationship for both active and inactive galaxies can therefore provide information about the parallel evolution of black holes and their host galaxies. By exploring the origin of the scaling relation (Woo et al. 2006; Kim et al. 2008) at high redshift (Peng et al. 2006), and within active galaxies (McLure & Dunlop 2002; Bettoni et al. 2003; Gaskell & Kormendy 2009), one can study the evolution of SMBHs with time in comparison with the spheroid evolution. Bennert et al. (2010) found no change for evolution of the $M_{\text{bh}}-L_{\text{tot}}$ relation up to $z=1$, in contradiction with the $M_{\text{bh}}-L_{\text{sph}}$ evolution. Further research of SMBH evolution shows that up to $z\sim 3$ host galaxies at fixed M_{bh} are less massive as compared to local galaxies (Treu et al. 2007; Jahnke et al. 2009). This indicates SMBHs in early-type galaxies have reached their final mass during the very earliest phases of galaxy evolution (Ivanov &

¹ Some other properties known to correlate with SMBH mass are the mean velocity dispersion (Tremaine et al. 2002) and the stellar mass (Häring & Rix 2004)

Alonso-Herrero 2003). As a result the $M_{\text{bh}}/M_{\text{gal}}$ should be larger compared with the local ratio (Greene et al. 2010), an outcome confirmed by QSO observations up to $z\sim 6$ (Walter et al. 2004; Shields et al. 2006; McLeod & Bechtold 2009). However, other studies argue that this result may arise due to a selection bias (Borys et al. 2005; Alexander et al. 2008).

Another aspect of the $M_{\text{bh}}-L$ relation is the behaviour at the low luminosity end. Do SMBHs exist in low-mass galaxies (Merritt et al. 2001) or is there a lower galaxy mass limit at which we can detect a SMBH. Hu (2009, hereafter H09) argue that bulge-less galaxies (or pseudobulges) follow a distinct relation while Greene et al. (2008) showed that a classical bulge is not necessary for a SMBH to exist. Pseudobulges are central components of late type galaxies with disk features and it is believed that they follow a separate formation path to the classical bulges with which they can coexist. For a review of the properties of pseudobulges see Kormendy & Kennicutt (2004).

The first estimation of the $M_{\text{bh}}-L$ relation in the near-IR was established by Marconi & Hunt (2003) using three band images from the Two Micron All Sky Survey (2MASS)² for a sample of 37 early- and late- type galaxies. The intrinsic scatter of their correlation ranges from $\sim 0.5\text{dex}$ to $\sim 0.3\text{dex}$ depending on the subsample selection. Graham (2007) refined the Marconi & Hunt (2003) $M_{\text{bh}}-L$ relation by using updated M_{bh} measurements and modifying the photometry of the data set and finding an intrinsic scatter of $\sim 0.30\text{dex}$.

More recently and in addition to the $M_{\text{bh}}-L$ relation Graham & Driver (2007, hereafter GD07 following on from Graham et al. 2001) found a relation between the galaxy light concentration n (Sérsic index) and M_{bh} with a comparable intrinsic scatter of 0.31dex . In the review by Novak et al. (2006) the $M_{\text{bh}}-n$ relation was shown to be as accurate on predicting M_{bh} as the $M_{\text{bh}}-\sigma$ relations.

Graham et al. (2007) and Vika et al. (2009) applied both the $M_{\text{bh}}-n$ and $M_{\text{bh}}-L$ relations respectively to derive the nearby SMBH mass functions for the Millennium Galaxy Catalogue (Liske et al. 2003; Driver et al. 2005) and derived individual SMBH mass measurements for a sample of 1743 galaxies. While the mass functions agreed well within the cited errors, the comparison of the derived SMBH masses on a galaxy by galaxy basis showed a low consistency between the two predictors. They explained that the lack of correlation is in part due to the scatter introduced by combining elliptical and disk galaxies, the uncertainty of separating the bulge component from the disk component, and due to the intrinsic scatter of the $M_{\text{bh}}-L, n$ correlations at optical wavelengths.

In this paper we aim to reconstruct the $M_{\text{bh}}-L, n$ relations in the near-IR by using high resolution UKIRT Infrared Deep Sky Survey (UKIDSS, Lawrence et al. 2007) images which extend significant deeper ($\sim 2\text{mag}/\text{arcsec}^2$) than the previous studies based on 2MASS. We specifically choose near-IR photometry because galaxy profiles should be less perturbed by young star populations and by dust attenuation relative to optical passbands (Driver et al. 2008). Thereby yielding a lower intrinsic scatter and enabling more accurate SMBH mass function determinations from the ap-

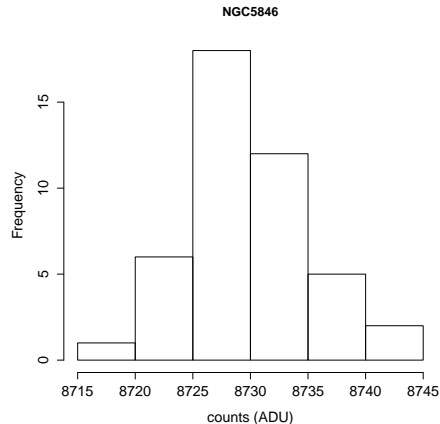


Figure 1. The distribution of the sky background for the NGC5846. The mean sky value is 8730 ADU with $\sigma = 6$.

plication of these relations to large surveys (e.g. GAMA see Driver et al. 2009).

Section 2 describes the data selection and the data reduction. Section 3 describes the methodology for measuring 2D radial surface-brightness profiles for our 29 galaxies using GALFIT3 (Peng et al. 2010) and presents information from the literature for our sample. In Section 4 we explore the $M_{\text{bh}}-L, n$ correlations and compare with previous studies. Finally, Section 5 summarises our conclusions and suggests possible direction for further study.

2 DATA REDUCTION

We extract calibrated K-band images from UKIDSS for 29 galaxies for which SMBH masses have been measured. These galaxies are a subsample of the host galaxy population, where the mass of the SMBH has been measured using a direct method. The full sample consists of 86 galaxies with SMBHs and 9 galaxies with intermediate massive black holes (IMBH), as presented by GO10 and references therein.

The wide-field images were obtained using the Wide Field Infrared Camera (WFCAM) (Casali et al. 2007) on the 3.8-m United Kingdom Infra-red Telescope (UKIRT) as part of the Large Area Survey UKIDSS-LAS (Lawrence et al. 2007). The pixel size of each detector is 0.4 arcsec with a gain of $4.5 e^-/\text{ADU}$ and a read noise of 25 ADU.

The properties of our galaxy sample are listed in Table 1. We include galaxies with SMBH masses measured with stellar kinematics, gas kinematics, water masers, stellar proper motion and reverberation mapping (see Table 6). The masses for NGC2778, NGC4473, NGC4564, NGC4697 and NGC5845 have been modified from their initial published values due to an update of their distances (see GO10). Our sample includes 15 elliptical galaxies and 14 disk galaxies (see Table 1).

We also include for reference only the Milky Way parameters derived from other studies. In particular, the SMBH mass is $(4.3 \pm 0.3)10^6 M_{\odot}$ for a distance of 0.0083Mpc (Gillessen et al. 2009), the bulge luminosity is $(4.0 \pm 1.2)10^8 L_{\odot}$ at $2.2\mu\text{m}$ (Dwek et al. 1995) and the Sérsic index $1.32^{+0.26}_{-0.22}$ (Kent et al. 1991; Graham & Driver 2007).

² Jarrett et al. (2000)

Table 1. Galaxy Sample; Column(1): Galaxy name; Column(2) and (3): equatorial coordinates (J2000); Column(4) and (5): K-Band and B-Band magnitudes from the SIMBAD Astronomical Database; Column(6): reddening estimate E(B-V) from Schlegel et al. (1998); Column(7): Hubble type from NED (and in bracket from GO10) ; Column(8): redshift from the NED; Column(9): Distance from Graham (2008); Column(11): Activity (Sy:Seyfert, NLRG:Narrow Line Radio Galaxy, HII:Nuclear HII regions, L:Low Ionisation Nuclear Emission-Line Regions,LLAGN:low-luminosity AGN.

Galaxy Name (1)	RA (J2000) (2)	DEC (J2000) (3)	K (mag) (4)	B (mag) (5)	A _k (mag) (6)	Type (7)	Redshift (8)	Activity (9)
NGC221	00 42 41.8	+40 51 57.2	5.09	9.2	0.057	cE2 (S0)	-0.0006	-
NGC863	02 14 33.56	-00 46 00.0	9.54	14.0	0.013	SA(s)a	0.02638	Sy1-2
NGC1068	02 42 40.83	-00 00 48.4	5.79	9.7	0.012	SAb	0.00379	Sy1-2
NGC2778	09 12 24.35	+35 01 39.4	9.514	13.1	0.008	E (SB0)	0.00683	-
NGC2960	09 40 36.46	+03 34 36.6	9.783	13.6	0.016	Sa	0.01645	Sy3
NGC3245	10 27 18.52	+28 30 24.8	7.862	11.6	0.009	SA(r) (S0)	0.00438	HII L
NGC4258	12 18 57.54	+47 18 14.3	5.464	9.6	0.006	SABbc	0.00149	Sy1
NGC4261	12 19 23.21	+05 49 29.7	7.26	12.0	0.006	E2	0.00746	Sy3-L
NGC4303	12 21 55.03	+04 28 28.7	6.843	10.9	0.008	SAB(rs)bc	0.00522	HII Sy2
NGC4342	12 23 39.12	+07 03 12.9	9.023	13.0	0.008	SO	0.0025	-
NGC4374	12 25 03.74	+12 53 13.1	6.222	10.8	0.015	E1	0.00353	Sy2-L
NGC4435	12 27 40.60	+13 04 44.4	7.297	11.9	0.011	SB(s) (SB0)	0.00267	-
NGC4459	12 29 00.13	+13 58 42.5	7.152	11.6	0.017	SA0	0.00403	HII L
NGC4473	12 29 48.95	+13 25 46.1	7.157	11.2	0.010	E5	0.00748	-
NGC4486	12 30 49.42	+12 23 28.0	5.812	10.4	0.008	cD,E0	0.00436	NLRG-Sy
NGC4486a	12 30 57.89	+12 16 13.7	11.2	9.01	0.009	E2	0.00050	-
NGC4486b	12 30 31.82	+12 29 25.9	10.09	14.5	0.008	cE0	0.00519	-
NGC4552	12 35 40	+12 33 22	6.728	11.1	0.015	E1 (S0)	0.00113	HII Sy2-L
NGC4564	12 36 27.01	+11 26 18.8	7.937	12.2	0.012	E6 (S0)	0.00380	-
NGC4596	12 39 56.16	+10 10 32.4	7.463	12.4	0.008	SB(r)0+	0.00623	L
NGC4621	12 42 02	+11 38 45	6.746	11.0	0.012	E5	0.00137	-
NGC4649	12 43 40.19	+11 33 08.9	5.739	10.3	0.010	E2	0.00372	-
NGC4697	12 48 35.7	-05 48 03	6.367	11.0	0.011	E6	0.00414	LLAGN
NGC5576	14 21 03.7	+03 16 16	7.827	11.9	0.011	E3	0.00496	-
NGC5813	15 01 11.3	+01 42 06	7.413	12.5	0.021	E1-2	0.00658	L
NGC5845	15 06 00.9	+01 38 01.4	9.112	13.8	0.020	E	0.00483	-
NGC5846	15 06 29.4	+01 36 19	6.935	11.9	0.020	E0	0.00571	HII L
NGC7052	21 18 33.1	+26 26 48	8.574	14.0	0.046	E	0.0241	-
UGC9799	15 16 44.6	+07 01 16.3	9.548	14.8	0.014	cD;E	0.0345	Sy2

2.1 Sky

The accuracy to which we can determine the sky background dictates the depth to which we can profile each galaxy. We measure the sky background by manually placing 40 - 50 boxes (10 x 10 pixels) at locations around each galaxy using the IRAF task imexamine. The sky value we then adopt is the mean of the median values from each box (see Figure 1 for details). The boxes are selected to lie away from stars, the faint halo of the galaxy, neighbouring galaxies that may exist and to be uniformly distributed around each image.

Some images (NGC2778, NGC3245, NGC4258, NGC7052) have a noticeable background gradient. We correct the gradient with the use of a SExtractor (Bertin & Arnouts 1996) fully resolved background map. To ensure that the subtraction of the background map will not deteriorate the galaxy flux we first subtract the galaxy with the help of a model constructed with IRAF - ELLIPSE BMODEL. After we have removed the model we create a fully resolved background map which we subtract from the initial image. The sky background values derived from the method described above can be found in Table 2 and are used later as an input to GALFIT3. All background values have been independently checked using STARLINK - ESP -

HISTPEAK and agree within the quality errors. Nevertheless we do note in particular the extensive structure in the background of the NGC4486 possibly due to the UKIDSS reduction pipeline. The NGC4486 case will be discussed further in Section 4.4.

2.2 PSF

Two PSFs are created for each galaxy, based on stars taken from the same data frame and using the package IRAF DAOPHOT. The PSF model is described by a penny2 function. Penny2 has a Gaussian core and Lorentzian wings which are free to be tilted in different directions. We construct the PSF from a sample of 10-15 stars selected from each galaxy/image in interactive mode. A different set of stars is used for each PSF. Saturated stars, or stars very close to the galaxy with unclear background levels, are excluded from the sample. After the creation of the DAOPHOT PSF we use it to subtract all stars from the original image. The left panel and the middle panel of Figure 2 show an example galaxy image before and after removing the stars.

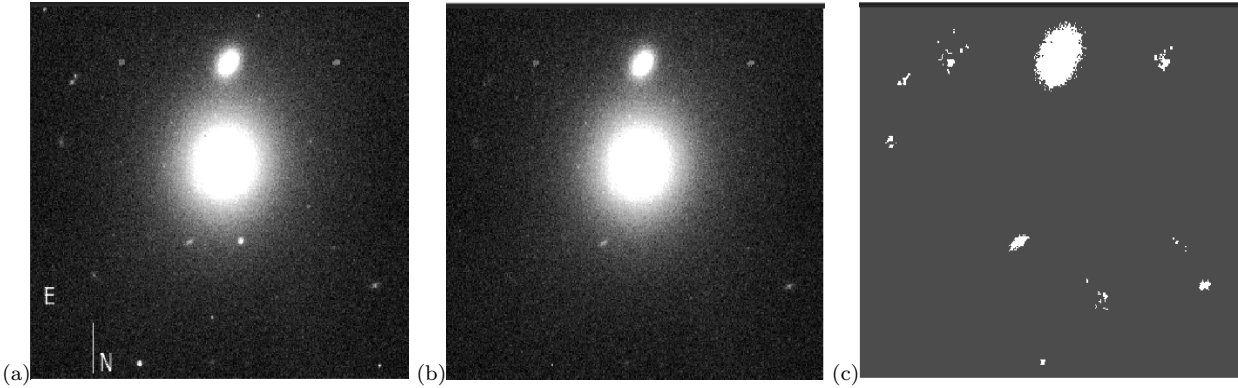


Figure 2. (a)K-band image of NGC5846 (b)The same image cleaned of background stars (c)The segmentation map. See Section 2 for details.

2.3 Image Masks

In some images the main galaxy is surrounded by satellite galaxies (e.g. UGC9799), bad pixels and saturated stars (e.g. NGC4459). The light distribution from the neighbouring galaxies and the area that the bad pixels cover cannot be cleaned with the same technique we used for the stars. In these cases we use an image mask that indicates to **GALFIT3** which areas of the image should not be used. We create these maps using **SExtractor** segmentation maps. The right panel of Figure 2 shows the **SExtractor** segmentation maps with pixels having a non zero value in the map being excluded from the fitting process.

3 PHOTOMETRIC DECOMPOSITION

We obtained the structural parameters of the host galaxies by performing **2D** fitting with **GALFIT3** (Peng et al. 2010). **GALFIT3** constructs analytic fits to galaxy images, allowing multi-component functions representing bulge, disk, bar, point-source and sky background components. **GALFIT3** uses the Levenberg-Marquardt technique to find the best fit. **GALFIT3** algorithm uses this nonlinear least-square technique to minimise the χ^2 residual between the galaxy image and the model by modifying all the free parameters and accepting them when the χ^2 is reduced. The normalised χ^2 is in the form:

$$\chi^2 = \frac{1}{n} \sum_1^{nx} \sum_1^{ny} \frac{(f_d(x, y) - f_m(x, y))^2}{\sigma(x, y)^2} \quad (1)$$

where n is the number of degrees of freedom in the fit, nx and ny are the x and y image dimensions, $f_d(x, y)$ is equal to the image flux at pixel (x, y) , and $f_m(x, y)$ is the sum of all the functions flux at the same pixel. The term $\sigma(x, y)$ is the Poisson error at each pixel position. The $\sigma(x, y)$ value can be estimated internally by **GALFIT3** based on the gain and read-noise values found in the header of each galaxy image or provided separately as a FITS image. Pixels contained in the mask image are not included in the χ^2 calculation.

The background is kept fixed to the value derived in Section 2.1. **GALFIT3** convolves the model with the point-spread function (PSF, see 2.2) to account for the results of atmospheric seeing. The free parameters for each component are the magnitude, the scalelength (r_s)/effective radius

(r_e), the concentration index n for the Sérsic models (Sérsic index), the axis ratio, and the position angle.

We modelled the radial light distribution of each galaxy using combinations of the following analytic functions: a Sérsic function (see Equation 2) to model elliptical galaxies, the bulge and/or the bar of lenticular and spiral galaxies; an Exponential function (Equation 2 where $n=1$) to model the disk of the galaxy and a Moffat function to model/mask the central part of one elliptical galaxy. For some bar-less disk galaxies the combination of a Sérsic plus an exponential component was insufficient to model the galaxy. In these cases we modelled the galaxies with a combination of two Sérsic functions. The Sérsic (1968) function is given by:

$$I(r) = I_e \exp \left\{ -b_n \left[\left(\frac{r}{r_e} \right)^{1/n} - 1 \right] \right\} \quad (2)$$

where I_e is the intensity at the effective radius (r_e), n is the Sérsic index and b_n is a function of n . The value of b_n can be derived from $\Gamma = 2\gamma(2n, b_n)$ and is used so that the effective radius encloses half of the total luminosity (see Graham & Driver 2005). When the Sérsic index is fixed to $n = 4, 1$ or 0.5 the Sérsic profile is identical to the well known de Vaucouleurs, exponential or Gaussian profile, respectively.

For the first run of **GALFIT3** we performed a single Sérsic model fit for all galaxies assuming that we can describe the distribution of light with a single component. The first run used initial values for the free parameters as implied by **SExtractor**. The magnitudes derived from the single Sérsic model were compared with the 2MASS magnitudes. The 2MASS magnitudes agreed with our single component magnitudes except for two galaxies, NGC4343 and NGC4486A (see Figure 3). For those cases where an additional component was required, either due to a poor Sérsic fit or an obvious disk in the images, a second run was conducted. The output parameters of the first run were then used as input parameters for the second run of **GALFIT3**. The second run used two-component (i.e. Sérsic bulge - exponential disk) for disk galaxies. The Sérsic bulge plus exponential disk model for the lenticular galaxy NGC4564 was still deficient and so a double Sérsic model was adopted for a third run. Note that the resulting Sérsic index for the disk of this galaxy was found to be 1.3 which is plausibly close to the value of the exponential function ($n = 1$).

In one case, the disk galaxy NGC4459 the Sérsic plus

Table 2. Galaxy Sample. The background is the mean value of fifty median sky values. Each median value has been estimated for a box of 100 pixels. The stddev is the standard deviation of the mean background value.

Galaxy Name (1)	Seeing (pixel) (2)	background (3)	stddev (4)	Exposure time (sec) (5)	Survey (6)	Telescope/ Instrument (7)
NGC 221	4.6	6540	8	10	SERV/1652	UKIRT/WFCAM
NGC 863	2.1	6606	3	10	LAS	UKIRT/WFCAM
NGC 1068	2.7	5945	5	10	LAS	UKIRT/WFCAM
NGC 2778	2.3	10723	1.2	10	B2	UKIRT/WFCAM
NGC 2960	1.9	4740	2	10	LAS	UKIRT/WFCAM
NGC 3245	1.9	10210	2	10	B2	UKIRT/WFCAM
NGC 4258	2.5	10635	2	10	B2	UKIRT/WFCAM
NGC 4261	1.4	5453	3	10	LAS	UKIRT/WFCAM
NGC 4303	1.7	6036	3	10	LAS	UKIRT/WFCAM
NGC 4342	1.1	5407	2	10	LAS	UKIRT/WFCAM
NGC 4374	2.8	5829	1.4	10	B2	UKIRT/WFCAM
NGC 4435	1.5	5782	5	10	LAS	UKIRT/WFCAM
NGC 4459	1.8	5402	3	10	LAS	UKIRT/WFCAM
NGC 4473	1.9	5368	4	10	LAS	UKIRT/WFCAM
NGC 4486	1.6	5580	9	10	LAS	UKIRT/WFCAM
NGC 4486a	1.2	5615	4	10	LAS	UKIRT/WFCAM
NGC 4486b	1.2	5581	5	10	LAS	UKIRT/WFCAM
NGC 4552	1.6	5612	4	10	LAS	UKIRT/WFCAM
NGC 4564	1.5	5123	4	10	LAS	UKIRT/WFCAM
NGC 4596	2.1	3316	2	10	LAS	UKIRT/WFCAM
NGC 4621	2.1	5117	3	10	LAS	UKIRT/WFCAM
NGC 4649	3.1	5258	5	10	LAS	UKIRT/WFCAM
NGC 4697	2.9	7449	3	10	B2	UKIRT/WFCAM
NGC 5576	2.6	5465	3	10	LAS	UKIRT/WFCAM
NGC 5813	1.9	7477	5	10	LAS	UKIRT/WFCAM
NGC 5845	2.0	8722	4	10	LAS	UKIRT/WFCAM
NGC 5846	1.8	8730	6	10	LAS	UKIRT/WFCAM
NGC 7052	2.1	6630	1.3	10	B2	UKIRT/WFCAM
UGC 9799	3.3	7377	2	10	LAS	UKIRT/WFCAM

disk fit was not sufficient to model the galaxy. After trying to model the galaxy by applying a single Sérsic model or combining extra functions we conclude that NGC4459 can be modelled better with a combination of a Sérsic function and a Moffat function. The Moffat function in `GALFIT3` has five free parameters: the total magnitude, the FWHM, the beta powerlaw, the axis ratio and the position angle. We fixed the FWHM and the beta parameter to values that we derived through the task `IRAF/psfmeasure`.

As described above, the outputs of the second run were used as input for the third run for galaxies whose residuals implied the existence of a bar. We applied a third run to galaxies with a bar component by using a three component model, i.e., Sérsic bulge - Exponential disk - Sérsic bar.

An additional run was also applied to active galaxies (as indicated by X-ray or Radio observations) that have a bright nucleus in near-IR (corresponding to a point source at our resolution). These galaxies are NGC863, NGC4258, NGC4303 and NGC4435. In these cases we model the nucleus as a PSF. It is not always clear whether introducing the PSF component improves the model or not and for this reason we provide two models for some active galaxies, one with and one without the PSF. Table 4 lists the main profile for each galaxy, which is used to derive the $M_{\text{bh}}-L, n$ relations while Table 5 shows the alternative profile information.

Massive elliptical and bulge galaxies often exhibit par-

tially depleted cores (i.e. deviations of the profile in the inner regions), this phenomena is well known and the innermost regions (1-5 per cent of the effective radius) often deviate, see for example Kormendy et al. (2009) and Glass et al. (2011). While there is relatively little flux involved their presence can cause particular difficulties in measuring an accurate Sérsic index. In Section 3.2 we present different methods used by previous studies to fit the core galaxies. `GALFIT3` does not provide a function to model the depleted cores but if we ignore the existence of the core structure and model the core galaxies with a single Sérsic model we will erroneously weight the fit to model the inner high signal-to-noise core. In these galaxies where the original profiles showed distinct departures in the inner regions we elect to mask. For these systems, indicated in Table 3, we implement a mask and re-profile and gradually increase the mask size until a stable outcome is found. Table 3 Col 3 shows the final mask sizes in units of the effective radius for each of our galaxies and no obvious correlation or rule of thumb is seen. We conclude that masking is critical for the recovery of an accurate Sérsic index but actually affects the bulge luminosity relatively little as the majority of the flux lies outside the core region. Also in the case of some bright galaxies the center of the galaxy has been saturated and as a result an artificial drop of counts appears. Here too we overcome the problem of the saturated area by masking the data. The galaxies to which a core mask has been applied are NGC1068, NGC221,

Table 3. Mask size of the inner regions for the galaxies for which their profile deviates from the Sérsic model. In the case of NGC1068 the saturated AGN has been masked while in the case of the NGC4486A the central area of the galaxy has been masked due to the existence of a bright star.

Galaxy Name (1)	Mask (arcsec) (2)	Mask/ r_{eff} (3)
NGC 221	2.75	15%
NGC 1068	0.6	saturated area
NGC 4261	1.0	4%
NGC 4374	1.0	3%
NGC 4473	1.4	6%
NGC 4486	3.8	10%
NGC 4486A	~5	saturated area
NGC 4621	1.8	3%
NGC 4649	2.6	5.6%
NGC 5576	2.0	11%
NGC 5813	1.0	1%
NGC 5846	2.6	5.6%
UGC 9799	1.0	3%

NGC4261, NGC4374, NGC4473, NGC4486, NGC4486A, NGC4621, NGC4649, NGC5576, NGC5813, NGC5846 and UGC9799.

When the minimisation is complete, **GALFIT3** produces FITS files for the original image, the model, the residual and the individual images for each component. To visually examine the goodness of the fit we use **IRAF ELLIPSE** to produce a **1D** profile of both the input galaxy, the fit and the each sub-component. This process ensures that the data and models are inspected in an identical manner with the position angle and the axis ratio of the ellipses were fixed to the values that **GALFIT3** has estimated for the bulge/spheroid. We placed the resulting ellipses onto both the model image and the sub-component images of the model. With this test we can see if the azimuthally measured surface brightness along the major axis of the model is in agreement with the surface brightness profile of the galaxy, and also the contribution to the overall profile from each component. The derived surface brightness profiles are displayed in Figures 5-33 together with the image of the galaxy, the residual, the model, the sub-components and the PSF as indicated. It is important to stress that these profiles are *not* an output of **GALFIT3** but simply an inspection tool that process the original image and **GALFIT3** output in an identical manner.

The apparent magnitudes produced by **GALFIT3** are converted into absolute magnitudes using the values of distance (d) and extinction (A_K) as listed in Tables 1 and 6 respectively.

The faint limit in surface brightness to which our fits are deemed reliable varies for each image from 20.6 mag arcsec⁻² to 22.7 mag arcsec⁻². Five galaxies (NGC221, NGC2960, NGC4473, NGC4621 and UGC9799) in our sample are located at the edge of their cutout. These galaxies cannot be profiled "down to their faint surface brightness limit". After testing the model surface brightness profile with **IRAF ELLIPSE** following the method described above for these five galaxies we decided that their derived parameters are robust (see Figures 5,9,18,25 and 33).

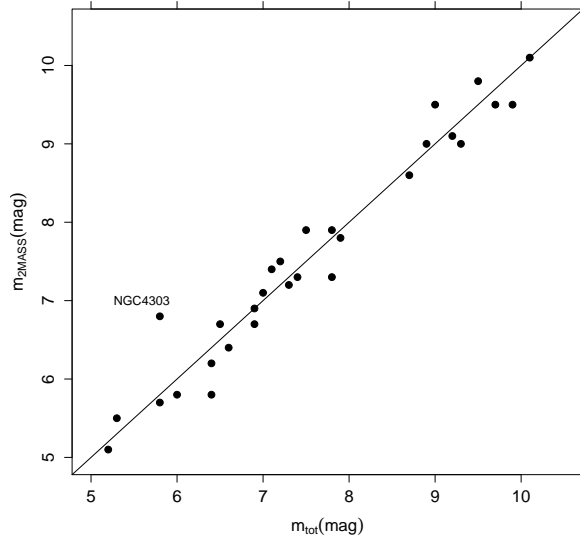


Figure 3. Correlation of this study single Sérsic apparent magnitudes versus the 2MASS apparent magnitudes.

3.1 Uncertainties

As we described in Section 2.1 we measured the background sky value as accurately as the image quality allows. However small variances on the mean sky value can significantly modify the output values. To calibrate the errors due to sky uncertainty we re-run **GALFIT3** using the best-fit values but changing the mean sky level by ± 1 sigma (where sigma is the uncertainty to which the mean sky level is known and listed in column 4 of Table 2). These two additional runs provide us with 1σ uncertainties for the magnitudes and the Sérsic indices required for deriving robust $M_{\text{bh}}-L, n$ relations (see Section 4.1).

The dominant systematic uncertainty is the validity of the choice of function(s) to describe the light distribution of a galaxy. Most galaxies in our sample leave residuals structures after removing the model, which may indicate smaller components that have not been modelled. In those cases where we see ambiguity we refit with/without the ambiguous component and report for completeness the alternative results in Table 5.

Finally we test the uncertainty introduced by the PSF. To explore this we re-run **GALFIT3** using the best-fit values but changing the PSF that **GALFIT3** use for convolution (see Figure 4 and Section 2.2). We find that the uncertainty introduced by the PSF ($\Delta M = 0.02$, $\Delta n = 0.2$) is small compared with the sky value uncertainty.

3.2 Notes on Modelling for Individual Galaxies

NGC221 (M32), M31s closest, satellite has a contaminated brightness profile due to the M31 disk. The contaminated light has a gradient from north-west, where it takes the maximum value, to south-east. Previous studies have excluded the inner 10 arcsec from their studies (Kent 1987; Graham 2002; Choi et al. 2002). Graham (2002) found that NGC221

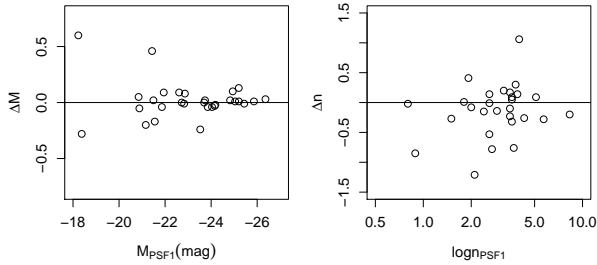


Figure 4. Left panel: Correlation of the spheroid absolute magnitudes of the best fit for two different PSFs. Right panel: The same as the left panel for Sérsic indexes. The black line in both panels is the 1-1 relation.

can be best profiled with a bulge/disk model ($n_{\text{bulge}} = 1.51$) while H09 found $n_{\text{bulge}} = 4.00$ plus disk³.

NGC863 (Mkr590) is a Seyfert 1 galaxy with a broad line spectrum.

NGC1068 (M77) is one of the most well studied barred spiral galaxies. The main bar was first observed in the near-IR by Scoville et al. (1988) while other studies have observed multiple bars (e.g. Erwin 2004). The nucleus hosts a Seyfert1-2 source with double jet observed in the radio (Gallimore et al. 1996) making the mid- and near- IR nuclei (inner 4 arcsec) appear extremely red (Alonso-Herrero et al. 1998; Bock et al. 2000). Drory & Fisher (2007) identify the existence of a pseudobulge based on the nuclear structure of the galaxy. H09 found $n_{\text{bulge}} = 1.51$, $n_{\text{bar}} = 0.7$ plus an exponential disk.

NGC2778 has been classified as an elliptical galaxy but GD07⁴ showed that it can be described better with a Sérsic bulge $n_{\text{bulge}} = 1.6$ plus a exponential disk which indicate a lenticular galaxy. This conclusion is also supported also from kinematical studies (Rix et al. 1999).

NGC2960 (Mrk1419) No previous information.

NGC3245 Kinematical studies show circularly rotating disks (Walsh et al. 2008). H09 found $n_{\text{bulge}} = 3.9$ plus an exponential disk.

NGC4258 (M106) A barred-spiral Seyfert galaxy that has been studied extensively over a broad band of wavelengths. The nucleus contains an edge-on warped accretion disk with radio jet (Herrnstein et al. 1997) and strong maser emission (Claussen et al. 1984). Both GD07 and H09 used a bulge/disk model and found $n_{\text{bulge}} = 2.04$, $n_{\text{bulge}} = 2.6$ respectively. Fisher & Drory (2010), found that $n_{\text{bulge}} = 2.8$ in mid-infrared and presented evidence of pseudobulge characteristics.

NGC4261 is the main elliptical galaxy in a group of 33 galaxies located behind the Virgo cluster (Huchra et al. 1983). The galaxy corresponds to the radio source (3C 270) which contains a pair of highly symmetric kpc-scale jets (Birkinshaw & Davies 1985) and an edge-on nuclear disk of gas and dust in the optical (Ferrarese et al. 1996; Jones

et al. 2000; Ferrarese et al. 2006). In X-ray it is possible that the galaxy hosts a heavily obscured AGN (Zezas et al. 2005). The isophotal analysis shows boxy isophotes at large radii both in the optical and near-IR bands (van den Bosch et al. 1994; Ferrarese et al. 1996; Quillen et al. 2000). GD07 derived a Sérsic index fit of $n = 7.3$.

NGC4303 (M61) is a double-barred AGN galaxy (Erwin 2004) with bright star-forming regions in a ring around the nucleus and in the spiral arms in the UV (Colina et al. 1997) and also visible in near-IR images (Möllenhoff & Heidt 2001). Weinzirl et al. (2009) performed a two dimensional bulge-disk-bar decomposition using GALFIT3 on H-band images and derived $n = 1.55, 1.0, 0.55$. Fisher & Drory (2010) showed that the spheroid component of the galaxy is a pseudobulge with $n_{\text{bulge}} = 1.7$.

NGC4342 is an S0 elongated galaxy with diskly isophotes (van den Bosch et al. 1994). Bosch et al. (1998) discovered the existence of a nuclear disk in addition to the outer disk through analysis of the rotation curve in HST/WFPC2 U-, V- and I-band imaging.

NGC4374 (M84, 3C272.1) is a radio elliptical galaxy. GD07 found $n_{\text{bulge}} = 4.97$ while Kormendy et al. (2009, hereafter KF09) found $n_{\text{bulge}} = 7.9$ after excluding the inner 4.2 arcsec⁵.

NGC4435 has boxy isophotes in the inner region and diskly isophotes at large radii (Ferrarese et al. 2006).

NGC4459 is a Virgo lenticular galaxy. H09 modelled NGC4459 with two components (bulge/disk $n_{\text{bulge}} = 2.5$). KF09 classified NGC4459 as an elliptical galaxy and estimated a Sérsic index of $n = 3.16$.

NGC4473 is an elliptical galaxy with primarily diskly isophotes (Bender et al. 1988; van den Bosch et al. 1994). Its unusual surface profile brightness has aroused plenty of interest, e.g., Byun et al. (1996); Ferrarese et al. (2006); Krajinović et al. (2006). The distribution of light in the inner part of the galaxy is dominated by a counter-rotating stellar disk (Cappellari et al. 2007). KF09 modelled the galaxy by excluding the inner 23 arcsec and measured a Sérsic index of $n = 4.0$ in agreement with the 2D profiling of H09. GD07 found a Sérsic index of $n = 2.73$.

NGC4486 (M87) is the second brightest elliptical Virgo galaxy and classified as a cD due to extra halo light originating from the cluster. Ferrarese et al. (2006) and GD07 agreed on their Sérsic index measurements 6.1 (using Sérsic-core model) and 6.8 respectively while KF09 profiled with the extra halo and found $n = 11.86$. A big discrepancy in the Sérsic values appears when we transferred to two dimensional profiling where both D’Onofrio (2001) and H09 found a significantly low Sérsic index $n = 3.0$.

NGC4486A has extra light from the nuclear disk visible in almost all wavelengths. In combination with a very bright star next to the centre it is difficult to provide a reliable fit at the centre. Ferrarese et al. (2006); Kormendy et al. (2009); Hu (2009) found Sérsic indices values 2.7, 2.04 and 4.2 respectively.

NGC4486B is a low-luminosity dwarf galaxy with extra light near the centre and characterised by a double core

³ H09 use the two dimensional bulge/disk decomposition program BUDDA and K-band images while Graham (2002) use the 1D algorithm UNCMND and R-band images.

⁴ GD07 derive their major-axis surface brightness profiles via fitting elliptical isophotes using IRAF ELLIPSE.

⁵ KF09 derive their major-axis surface brightness profiles via fitting elliptical isophotes allowing a boxy/disky parameter to vary (MIDAS/ESO).

(Lauer et al. 1996) which flattens the profile close to the nucleus. Due to its orbit around NGC4486, a fraction of the light from NGC4486b is actually halo light from its companion and consequently affects the surface brightness of NGC4486b. KF09 estimated a Sérsic index of $n = 2.2$ after modelling the additional light from NGC4486 and masking the inner 1.3 arcsec. Soria et al. (2006) found $n = 2.7$.

NGC4552 (M89) Caon et al. (1993) first profiled this S0 galaxy with a single Sérsic index of $n = 13.87$ excluding the inner 2 arcsec while KF09 applied the same model and found $n = 9.1$. Ferrarese et al. (2006) applied a core-Sérsic model and found $n_g = 7.1$. Finally in two-dimension modelling D’Onofrio (2001) and H09 used a bulge/disk model ($n_{\text{bulge}} = 4.2, 4.6$) yielding a much lower n value.

NGC4564 has been classified as elliptical in RC3 while Trujillo et al. (2004) classified it as an S0 galaxy. The existence of the disk is also verified by GD07 and KF09 with a bulge Sérsic index value of 3.15 and 4.69 respectively. Also H09 found $n_{\text{bulge}} = 3.6$ plus an exponential disk.

NGC4596 bar properties have been studied by Kent (1990) and Erwin (2005). H09 found $n_{\text{bulge}} = 3.3$, $n_{\text{bar}} = 1.0$ plus an exponential disk.

NGC4621 (M59) Ferrarese et al. (2006) and KF09 profiled NGC4621 with a single Sérsic index and found $n_{\text{bulge}} = 6.8$ and 5.36 respectively. While H09 applied a bulge/disk model and found $n_{\text{bulge}} = 4.1$.

NGC4649 Ferrarese et al. (2006) found $n_{\text{bulge}} = 4.7$ plus core while GD07 and H09 fitted single Sérsic model and derived $n_{\text{bulge}} = 6.04$ and 3.4 respectively.

NGC4697 GD07 measured $n = 4.0$ while H09 found $n_{\text{bulge}} = 3.0$ plus an exponential disk.

NGC5576 is an elliptical galaxy which Trujillo et al. (2004) profiled with both a single Sérsic model ($n = 4.47$) and a Sérsic plus core model ($n = 4.89$).

NGC5813 is an elliptical galaxy with a core (Lauer et al. 1995; Rest et al. 2001). H09 profiled with a bulge/disk model $n_{\text{bulge}} = 4.6$.

NGC5845 is a dwarf elliptical galaxy in the group of NGC5846 with an unusually high central surface brightness. It hosts a nuclear disk and dust disk that extends to 15 arcsec on the major axis (Quillen et al. 2000; Mahdavi et al. 2005). GD07 and Trujillo et al. (2004) performed **1D** profiling of the V-band images and derived a Sérsic index of $n = 3.22$ (single Sérsic fit) and $n = 2.88$ (Sérsic fit plus core fit) respectively. H09 found $n = 4.6$.

NGC5846 is the main galaxy in an isolated group of 250 galaxies (Mahdavi et al. 2005) with a compact radio core at the optical centre (Moellenhoff et al. 1992). Forbes et al. (1997) found slightly boxy isophotes in central regions while Rest et al. (2001) argued that due to strong dust filaments it is not possible to study the nucleus and have reliable information about the isophotal shape. H09 modelled the galaxy light profile with a single Sérsic and found $n = 3.1$.

NGC7052 is an isolated radio galaxy with an edge-on dust ring along the major axis (Nieto et al. 1990) and nuclear disk of gas/dust (de Juan et al. 1996) which affects the boxy/disky measurements of isophotes in the outer regions of the galaxy (Quillen et al. 2000). GD07 and H09 modelled the galaxy light profile and estimated Sérsic indices of $n = 4.55$ and $= 3.4$ respectively.

UGC9799 (3C 317) is the central elliptical galaxy (cD morphological class; cf. Seigar et al. 2007) of the cooling flow

cluster, Abell 2052. It features a central X-ray excess and is host to an active galactic nucleus (AGN) evident as a bright, steep-spectrum radio source (e.g. Zhao et al. 1993) with a compact optical counterpart (Castro-Rodríguez & Garzón 2003; Seigar et al. 2007). Seigar et al. (2007) and Donzelli et al. (2007) also identify a distinct outer halo to UGC 9799 (consistent with its classification as a cD morphological type) in Jacobus Kapteyn Telescope *R*-band and HST NICMOS *H*-band (F160W) imaging respectively. After masking the inner ~ 1 -2 arcsec (to exclude the central AGN) and modelling the outer halo with an exponential light distribution, these authors recovered Sérsic index fits of $n = 1.2$ and 2.3 to its major-axis surface brightness profile respectively⁶.

Our fits to all these galaxies are shown in Figures 5 - 33 and the results of our profiles are tabulated in Table 4. Where the number of components is ambiguous we show the alternative profiles and tabulate its results in Table 5.

4 RESULTS

4.1 Fitting Methodology

In Figure 34 we plot the black hole masses versus the absolute bulge/elliptical K-band magnitude of the host galaxies. The fitting algorithm used to estimate the linear $M_{\text{bh}}-L$ relation and the log-linear $M_{\text{bh}}-n$ relation is the regression analysis given in Tremaine et al. (2002)

$$\chi^2 = \sum_{i=1}^N \frac{(y_i - \alpha - \beta x_i)^2}{\delta y_i^2 + \beta^2 \delta x_i^2} \quad (3)$$

where $x = \log n$ or $x = M_{\text{K, sph}}$, $y = \log(M_{\text{bh}}/M_{\odot})$ and δy_i , δx_i are the errors of the x and y measurements. Tremaine et al. (2002) inserted the intrinsic scatter ϵ_0 of the $M_{\text{bh}}-L$, n correlations by replacing δy_i with $(\delta y_i^2 + \epsilon_0^2)^{1/2}$. Where ϵ_0 is computed by repeating the fit until $\chi^2/(N-2) = 1$. The uncertainty on the ϵ_0 is estimated when $\chi^2/(N-2) = 1 \pm \sqrt{2/N}$.

Here we assume that the errors cited in the literature are 1σ uncertainties if not clearly stated. We now implement a Monte Carlo method to derive the errors. To do this we randomly perturb each SMBH mass and the galaxy magnitude in each case assuming a Normal error distribution. We repeat the fit 1001 times, each time applying equation 3, assuming that the uncertainty is zero, consequently δy and δx are zero.

The final values for the intercept α and the slope β are then derived from the median value of the 1001 individual sets of α and β values while the δy and the δx are the standard deviations. We can see an illustration of the method in the bottom of the right panel of Figure 34. The 1001 red points shows the measurement distribution for NGC221 around the mean value. There are an equal number of points in each quadrant.

⁶ Both Seigar et al. (2007) and Donzelli et al. (2007) derived their major-axis surface brightness profiles via fitting of ‘perfect’ (i.e., non-boxy/disky) elliptical isophotes to their galaxy images using IRAF ELLIPSE.

4.2 Robustness of Mass Measurements

A number of galaxies (NGC863, NGC4435, NGC4486b and UGC9799) have poorly constrained mass measurements. NGC863 is the only galaxy in our sample for which the SMBH mass has been estimated via the method of reverberation mapping. Reverberation mapping masses use the local $M_{\text{bh}}-\sigma$ relation to normalise their values. Figure 34 shows that NGC863 is offset from the expected relation by ~ 1 dex while the virial mass estimation appears to be rather consistent with the $M_{\text{bh}}-L$ relation. NGC4435 and UGC9799 have only upper limit on their SMBH mass estimations. NGC4486b SMBH mass measurement has been characterised as weak while the mass estimation models show a possibility of zero mass black hole. For these reasons the above referred galaxies have been excluded from the following fits.

4.3 $M_{\text{bh}}-L$ correlation

Figure 34 shows the $M_{\text{bh}}-L$ distribution for our full sample with the error bars shown in the right panel and various symbols indicating the morphological characteristics in the left panel. Applying Equation 3 to our trustworthy sample of 25 galaxies we derive:

$$\log(M_{\text{bh}}/M_{\odot}) = -0.35(\pm 0.024)(M_{\text{K}} + 18) + 6.2(\pm 0.13) \quad (4)$$

with an intrinsic scatter of $0.52_{-0.06}^{+0.1}$ dex in $\log M_{\text{bh}}$. This level of intrinsic scatter is relatively high and may arise from the varied morphological mix of our sample (see Table 1).

If we exclude the barred galaxies (NGC1068, NGC4258, NGC4303 and NGC4596) for which bulge fluxes are consider the most uncertain, and the extreme outlying galaxy NGC4342 from the regression analysis we derive:

$$\log(M_{\text{bh}}/M_{\odot}) = -0.37(\pm 0.03)(M_{\text{K}} + 18) + 6.1(\pm 0.18) \quad (5)$$

with an intrinsic scatter of $0.43_{-0.06}^{+0.09}$ dex in $\log M_{\text{bh}}$ for a subsample of 20 galaxies.

Finally, if we additionally exclude the low quality image cD galaxy, NGC4486 (see §4.4), we find:

$$\log(M_{\text{bh}}/M_{\odot}) = -0.36(\pm 0.03)(M_{\text{K}} + 18) + 6.17(\pm 0.16) \quad (6)$$

with an intrinsic scatter of $0.40_{-0.06}^{+0.09}$ dex in $\log M_{\text{bh}}$ for a secure high quality subsample of 19 galaxies.

When we apply the equation to our elliptical subsample consisting of 13 galaxies (again excluding NGC4486) we obtain:

$$\log(M_{\text{bh}}/M_{\odot}) = -0.42(\pm 0.06)(M_{\text{K}} + 22) + 7.5(\pm 0.15) \quad (7)$$

with an intrinsic scatter of $0.31_{-0.047}^{+0.087}$ dex in $\log M_{\text{bh}}$.

The red dotted line in Figure 34 shows the Marconi & Hunt (2003) relation after Graham (2007) corrections have been applied. This relation has been derived from a sample of 26 galaxies (9 of which are within our sample) and has an intrinsic scatter of 0.35 dex (the best fit of Marconi & Hunt (2003) full sample, consisting of 37 galaxies gives an intrinsic scatter 0.51 dex). From Figure 34 we see that our $M_{\text{bh}}-L$ relation is found to be consistent with previous measurements. Previous near-IR $M_{\text{bh}}-L$ relations are based

on 2MASS data. The shallow nature of the 2MASS imaging makes it difficult to identify faint components of a galaxy. For instance Marconi & Hunt (2003) misclassified NGC221, NGC2778 and NGC4564 as elliptical galaxies.

We noticed that the intrinsic scatter of the $M_{\text{bh}}-L$ relation is increased when we include barred galaxies. The increased dispersion of the scatter could be the result of the uncertainty introduced by estimating the individual luminosity for each component. Also the barred galaxies in our sample have nuclei activity. Extracting the bulge luminosities for these galaxies is complex because of the contamination of the bulge flux from active nuclei.

In conclusion we find that our high quality data replicate but do not improve the intrinsic scatter suggesting a genuine spread in the data $\epsilon_0 = \pm 0.31$. We note the significant uncertainty when including multiply component systems $\epsilon_0 = \pm 0.52$.

4.4 $M_{\text{bh}}-n$ correlation

Figure 35 shows the M_{bh} as a function of Sérsic indices in the K-band. The sample selection is the same as that noted in §4.3. Contrary to expectations our Sérsic index values does not show strong correlation with M_{bh} .

In Figure 36 we compare our Sérsic indices with Sérsic indices from the literature. In the left panel of Figure 36 we plot M_{bh} versus the Sérsic indices found in the literature for 16 galaxies matching our sample. These measurements are derived for R, V- band images using one dimensional profiling (listed in Table 6). The right panel shows the M_{bh} versus this study's Sérsic indices. Individual comparisons for each galaxy's Sérsic index can be found in §3.2.

The tight relation between the M_{bh} and Sérsic index found in **1D** optical analysis disappears in our **2D** near-IR study. We notice that **2D** analysis appear to have an upper limit of $n \sim 5$. Especially, massive elliptical galaxies like NGC4261, NGC4486 and NGC452 appear to have small Sérsic indexes. In the case of NGC4486 we suspect that the sky gradient of the image obstruct us from fitting the halo of the galaxy. The discrepancy between the different studies therefore appear to be a result of either the method used to model the galaxy (i.e. 1D v 2D) and/or the transfer from optical wavelength to K-band images.

Kelvin et al. (in preparation) perform multi-wavelength **2D** profiling in nine bands, from u-band to K-band, with **GALFIT3**, finding no important change of Sérsic indices for early-type systems in moving from r-band to near-IR. However disks and disk components are noted to show an increase in Sérsic index with wavelength and lowering in half-light radii. It appears then that the distinction between disk and bulge is less pronounced in the near-IR data compared to the optical.

We believe that a further cause of the mismatch could be the different pixel weighting adopted by **1D** v **2D** studies. **GALFIT3** weights pixels using a sigma (weight) map. The sigma map shows the one standard deviation of counts at each pixel. Such maps can be created by the program itself or supplied by the user. We chose to follow **GALFIT3** manual suggestion and let the program create the maps internally (See Appendix A for details). The only input values are required for the sigma images to be produced internally are

the background sky value and the root-mean-square (RMS) scatter of the background sky value.

Another known source of uncertainty of the Sérsic index is the switch from major axis fitting to minor axis fitting (Caon et al. 1993). Ferrari et al. (2004) showed that major and minor axis Sérsic index mismatch occur when there are radial variations of the isophotal eccentricity.

Further work is required to investigate what causes the breakdown of the $M_{\text{bh}}-n$ correlation. Vika et al. (in preparation) will pursue this by exploring the photometric properties derived from **1D** and **2D** fits for a larger sample of ~ 200 elliptical galaxies and the contribution of different pixel weights.

Our conclusion is that the $M_{\text{bh}}-n$ relation is no longer clearly apparent in the high quality near-IR data. We believe that this is caused by a combination of the use of **2D** fitting in conjunction with the difficulty to distinguish the bulge and disk components in near-IR data. While we cannot rule out minor errors in the profiling process we have explored a variety of alternative fits with extensive masking. As the motivation was to derive an $M_{\text{bh}}-n$ relation suitable for application to automated **GALFIT3** analysis we must conclude that the $M_{\text{bh}}-n$ relation is unsuitable for such use either because of a breakdown of the relation when **2D** fitting is used or the excessive care required to mitigate the core deviations.

5 SUMMARY

One of the main motivations of this study was to derive $M_{\text{bh}}-L, n$ relations using high quality near-IR data and using the same methods that we will apply to the GAMA survey in order to derive the SMBH mass function (e.g. Vika et al. 2009). In this paper, we tested the $M_{\text{bh}}-L, n$ relations using updated SMBH masses and provide new estimations of the galaxy component luminosities and light profile shapes. We made use of K-band galaxy images for a sample of 29 galaxies taken by WFCAM as part of the UKIDSS-LAS.

We used **GALFIT3** to produce **2D** surface-brightness photometry on K-band images and decomposed the different components of the host galaxy. We carefully modelled all the components of each galaxy and derived estimates of the various structural parameters for each galaxy along with a concise discussion of each galaxy previous studies at optical wavelengths.

We have used 21 elliptical and disk systems with classical bulge galaxies to derive the $M_{\text{bh}}-L$ relation with intrinsic scatter of 0.41. We confirm a strong correlation between the central M_{bh} and its host galaxy's spheroid luminosity found from a number of previous studies. Overall, we see that the scatter of the $M_{\text{bh}}-L$ relation is much larger when we include bar galaxies and galaxies with active nuclei. We found no improvement of the intrinsic scatter for the $M_{\text{bh}}-L$ relation by using higher quality data which may indicate that we have reached the physical limit to which one we can constrain the $M_{\text{bh}}-L$ relation.

Using the same sample of galaxies we failed to find a clear $M_{\text{bh}}-n$ correlation but we noticed that the Sérsic index can vary significantly from study to study. The available data are inadequate for deriving accurate outcomes for the different Sérsic index values. Our best explanation is that the

mismatch arises from the different weighting of pixel during the fit that each study uses. Further comparison of **1D** analysis versus **2D** analysis is required to fully understand this result.

In conclusion we have established an $M_{\text{bh}}-L$ relation based on **GALFIT3 2D** profiling of near-IR data which we will shortly apply to the GAMA dataset (Vika et al in preparation).

ACKNOWLEDGMENTS

This work is based in part on data obtained as part of the UKIRT Infrared Deep Sky Survey. The UKIDSS project is defined in Lawrence et al. 2007. UKIDSS uses the UKIRT Wide Field Camera (WFCAM; Casali et al. 2007) and a photometric system described in Hewett et al. 2006. The pipeline processing and science archive are described in Irwin et al (2010, in preparation) and Hambly et al. 2008. We thank the referee for helpful suggestions that improve this paper.

REFERENCES

- Alexander D. M., Brandt W. N., Smail I., Swinbank A. M., Bauer F. E., Blain A. W., Chapman S. C., Coppin K. E. K., et al., 2008, *AJ*, 135, 1968
- Alonso-Herrero A., Simpson C., Ward M. J., Wilson A. S., 1998, *ApJ*, 495, 196
- Barth A. J., Sarzi M., Rix H., Ho L. C., Filippenko A. V., Sargent W. L. W., 2001, *ApJ*, 555, 685
- Bender R., Doebereiner S., Moellenhoff C., 1988, *AAPS*, 74, 385
- Bennert V. N., Treu T., Woo J., Malkan M. A., Le Bris A., Auger M. W., Gallagher S., Blandford R. D., 2010, *ApJ*, 708, 1507
- Bertin E., Arnouts S., 1996, *A&AS*, 117, 393
- Bettoni D., Falomo R., Fasano G., Govoni F., 2003, *AAP*, 399, 869
- Birkinshaw M., Davies R. L., 1985, *ApJ*, 291, 32
- Bock J. J., Neugebauer G., Matthews K., Soifer B. T., Becklin E. E., Ressler M., Marsh K., Werner M. W., et al., 2000, *AJ*, 120, 2904
- Borys C., Smail I., Chapman S. C., Blain A. W., Alexander D. M., Ivison R. J., 2005, *ApJ*, 635, 853
- Bosch F. C., Jaffe W., van der Marel R. P., 1998, *MNRAS*, 293, 343
- Byun Y.-I., Grillmair C. J., Faber S. M., Ajhar E. A., Dressler A., Kormendy J., Lauer T. R., Richstone D., Tremaine S., 1996, *AJ*, 111, 1889
- Caon N., Capaccioli M., D'Onofrio M., 1993, *MNRAS*, 265, 1013
- Cappellari M., Bacon R., Davies R. L., de Zeeuw P. T., Emsellem E., Falcón-Barroso J., Krajnović D., Kuntschner H., et al., 2008, in M. Bureau, E. Athanassoula, & B. Barbuy ed., *IAU Symposium Vol. 245 of IAU Symposium, Supermassive black holes from oasis and sauron integral-field kinematics*. pp 215–218
- Cappellari M., Emsellem E., Bacon R., Bureau M., Davies R. L., de Zeeuw P. T., Falcón-Barroso J., Krajnović D., et al., 2007, *MNRAS*, 379, 418

- Casali M., Adamson A., Alves de Oliveira C., Almaini O., Burch K., Chuter T., Elliot J., 2007, *AAP*, 467, 777
- Castro-Rodríguez N., Garzón F., 2003, *AAP*, 411, 55
- Choi P. I., Guhathakurta P., Johnston K. V., 2002, *AJ*, 124, 310
- Claussen M. J., Heiligman G. M., Lo K. Y., 1984, *Nat*, 310, 298
- Coccatto L., Sarzi M., Pizzella A., Corsini E. M., Dalla Bontà E., Bertola F., 2006, *MNRAS*, 366, 1050
- Colina L., Garcia Vargas M. L., Mas-Hesse J. M., Alberdi A., Krabbe A., 1997, *ApJL*, 484, L41
- Cretton N., van den Bosch F. C., 1999, *ApJ*, 514, 704
- Dalla Bontà E., Ferrarese L., Corsini E. M., Miralda-Escudé J., Coccatto L., Sarzi M., Pizzella A., Beifiori A., 2009, *ApJ*, 690, 537
- de Juan L., Colina L., Golombek D., 1996, *AAP*, 305, 776
- D'Onofrio M., 2001, *MNRAS*, 326, 1517
- Donzelli C. J., Chiaberge M., Macchetto F. D., Madrid J. P., Capetti A., Marchesini D., 2007, *ApJ*, 667, 780
- Driver S. P., Liske J., Cross N. J. G., De Propriis R., Allen P. D., 2005, *MNRAS*, 360, 81
- Driver S. P., Norberg P., Baldry I. K., Bamford S. P., Hopkins A. M., Liske J., Loveday J., Peacock J. A., et al., 2009, *Astronomy and Geophysics*, 50, 050000
- Driver S. P., Popescu C. C., Tuffs R. J., Graham A. W., Liske J., Baldry I., 2008, *ApJ*, 678, L101
- Drory N., Fisher D. B., 2007, *ApJ*, 664, 640
- Dwek E., Arendt R. G., Hauser M. G., Kelsall T., Lisse C. M., Moseley S. H., Silverberg R. F., Sodroski T. J., Weiland J. L., 1995, *ApJ*, 445, 716
- Erwin P., 2004, *AAP*, 415, 941
- Erwin P., 2005, *MNRAS*, 364, 283
- Ferrarese L., Côté P., Jordán A., Peng E. W., Blakeslee J. P., Piatek S., Mei S., Merritt D., Milosavljević M., Tonry J. L., West M. J., 2006, *ApJS*, 164, 334
- Ferrarese L., Ford H. C., Jaffe W., 1996, *ApJ*, 470, 444
- Ferrarese L., Freedman W. L., Hill R. J., Saha A., Madore B. F., Kennicutt Jr. R. C., Stetson P. B., Ford H. C., Graham J. A., Hoessel et al., 1996, *ApJ*, 464, 5688
- Ferrari F., Dottori H., Caon N., Nobrega A., Pavani D. B., 2004, *MNRAS*, 347, 824
- Fisher D. B., Drory N., 2010, *ApJ*, 716, 942
- Forbes D. A., Brodie J. P., Huchra J., 1997, *AJ*, 113, 887
- Gallimore J. F., Baum S. A., O'Dea C. P., Pedlar A., 1996, *ApJ*, 458, 136
- Gaskell C. M., Kormendy J., 2009, in S. Jogee, I. Marinova, L. Hao, & G. A. Blanc ed., *Astronomical Society of the Pacific Conference Series Vol. 419 of Astronomical Society of the Pacific Conference Series, An Improved Black Hole Mass-Bulge Luminosity Relationship for AGNs*. p. 388
- Gebhardt K., Richstone D., Tremaine S., Lauer T. R., Bender R., Bower G., Dressler A., Faber S. M., Filippenko A. V., Green R., Grillmair C., Ho L. C., Kormendy J., Magorrian J., Pinkney J., 2003, *ApJ*, 583, 92
- Gebhardt K., Thomas J., 2009, *ApJ*, 700, 1690
- Gillessen S., Eisenhauer F., Fritz T. K., Bartko H., Dodds-Eden K., Pfuhl O., Ott T., Genzel R., 2009, *ApJL*, 707, L114
- Glass L., Ferrarese L., Côté P., Jordán A., Peng E., Blakeslee J. P., Chen C.-W., Infante L., Mei S., Tonry J. L., West M. J., 2011, *ApJ*, 726, 31
- Graham A. W., 2002, *ApJL*, 568, L13
- Graham A. W., 2007, *MNRAS*, 379, 711
- Graham A. W., 2008, *Publications of the Astronomical Society of Australia*, 25, 167
- Graham A. W., Driver S. P., 2005, *Publications of the Astronomical Society of Australia*, 22, 118
- Graham A. W., Driver S. P., 2007, *ApJ*, 655, 77
- Graham A. W., Driver S. P., Allen P. D., Liske J., 2007, *MNRAS*, 378, 198
- Graham A. W., Erwin P., Caon N., Trujillo I., 2001, *ApJL*, 563, L11
- Graham A. W., Onken C. A., Athanassoula E., Combes F., 2010, *ArXiv e-prints*
- Greene J. E., Ho L. C., Barth A. J., 2008, *ApJ*, 688, 159
- Greene J. E., Peng C. Y., Ludwig R. R., 2010, *ApJ*, 709, 937
- Gültekin K., Richstone D. O., Gebhardt K., Lauer T. R., Pinkney J., Aller M. C., Bender R., Dressler A., et al., 2009, *ApJ*, 695, 1577
- Gültekin K., Richstone D. O., Gebhardt K., Lauer T. R., Tremaine S., Aller M. C., Bender R., Dressler A., et al., 2009, *ApJ*, 698, 198
- Hambly N. C., Collins R. S., Cross N. J. G., Mann R. G., Read M. A., Sutorius E. T. W., Bond I., Bryant J., et al., 2008, *MNRAS*, 384, 637
- Häring N., Rix H. W., 2004, *ApJ*, 604, L89
- Henkel C., Braatz J. A., Greenhill L. J., Wilson A. S., 2002, *AAP*, 394, L23
- Herrnstein J. R., Moran J. M., Greenhill L. J., Diamond P. J., Inoue M., Nakai N., Miyoshi M., Henkel C., Riess A., 1999, *Nat*, 400, 539
- Herrnstein J. R., Moran J. M., Greenhill L. J., Diamond P. J., Miyoshi M., Nakai N., Inoue M., 1997, *ApJL*, 475, L17+
- Hewett P. C., Warren S. J., Leggett S. K., Hodgkin S. T., 2006, *MNRAS*, 367, 454
- Hu J., 2009, *ArXiv e-prints*
- Huchra J., Davis M., Latham D., Tonry J., 1983, *ApJS*, 52, 89
- Ivanov V. D., Alonso-Herrero A., 2003, *Ap&SS*, 284, 565
- Jahnke K., Bongiorno A., Brusa M., Capak P., Cappelluti N., Cisternas M., Civano F., Colbert J., et al., 2009, *ApJL*, 706, L215
- Jarrett T. H., Chester T., Cutri R., Schneider S., Skrutskie M., Huchra J. P., 2000, *AJ*, 119, 2498
- Jerjen H., Binggeli B., Barazza F. D., 2004, *AJ*, 127, 771
- Jones D. L., Wehrle A. E., Meier D. L., Piner B. G., 2000, *ApJ*, 534, 165
- Kent S. M., 1987, *AJ*, 94, 306
- Kent S. M., 1990, *MNRAS*, 247, 702
- Kent S. M., Dame T. M., Fazio G., 1991, *ApJ*, 378, 131
- Kim M., Ho L. C., Peng C. Y., Barth A. J., Im M., Martini P., Nelson C. H., 2008, *ApJ*, 687, 767
- Kormendy J., Bender R., Magorrian J., Tremaine S., Gebhardt K., Richstone D., Dressler A., Faber S. M., Grillmair C., Lauer T. R., 1997, *ApJL*, 482, L139+
- Kormendy J., Fisher D. B., Cornell M. E., Bender R., 2009, *ApJS*, 182, 216
- Kormendy J., Gebhardt K., 2001 Vol. 586, *Supermassive black holes in galactic nuclei*
- Kormendy J., Kennicutt Jr. R. C., 2004, *ARA&A*, 42, 603
- Kormendy J., Richstone D., 1995, *ARA&A*, 33, 581

- Krajnović D., Cappellari M., de Zeeuw P. T., Copin Y., 2006, *MNRAS*, 366, 787
- Lauer T. R., Ajhar E. A., Byun Y.-I., Dressler A., Faber S. M., Grillmair C., Kormendy J., Richstone D., Tremaine S., 1995, *AJ*, 110, 2622
- Lauer T. R., Tremaine S., Ajhar E. A., Bender R., Dressler A., Faber S. M., et al., 1996, *ApJL*, 471, L79
- Lawrence A., Warren S. J., Almaini O., Edge A. C., Hamblly N. C., Jameson R. F., Lucas P., Casali M., 2007, *MNRAS*, 379, 1599
- Liske J., Lemon D. J., Driver S. P., Cross N. J. G., Couch W. J., 2003, *MNRAS*, 344, 307
- Lodato G., Bertin G., 2003, *AAP*, 398, 517
- Macchetto F., Marconi A., Axon D. J., Capetti A., Sparks W., Crane P., 1997, *ApJ*, 489, 579
- Maciejewski W., Binney J., 2001, *MNRAS*, 323, 831
- Magorrian J., Tremaine S., Richstone D., Bender R., Bower G., Dressler A., Faber S. M., Gebhardt K., Green R., Grillmair C., Kormendy J., Lauer T., 1998, *AJ*, 115, 2285
- Mahdavi A., Trentham N., Tully R. B., 2005, *AJ*, 130, 1502
- Marconi A., Hunt L. K., 2003, *AJ*, 589, L21
- McLeod K. K., Bechtold J., 2009, *ApJ*, 704, 415
- McLure R. J., Dunlop J. S., 2002, *MNRAS*, 331, 795
- Merritt D., Ferrarese L., Joseph C. L., 2001, *Science*, 293, 1116
- Moellenhoff C., Hummel E., Bender R., 1992, *AAP*, 255, 35
- Möllenhoff C., Heidt J., 2001, *AAP*, 368, 16
- Nieto J. L., McClure R., Fletcher J. M., Arnaud J., Bacon R., Bender R., Comte G., Poulain P., 1990, *AAP*, 235, L17
- Novak G. S., Faber S. M., Dekel A., 2006, *ApJ*, 637, 96
- Nowak N., Saglia R. P., Thomas J., Bender R., Pannella M., Gebhardt K., Davies R. I., 2007, *MNRAS*, 379, 909
- Pastorini G., Marconi A., Capetti A., Axon D. J., Alonso-Herrero A., Atkinson J., Batcheldor D., Carollo C. M., et al., 2007, *AAP*, 469, 405
- Peng C. Y., Ho L. C., Impey C. D., Rix H.-W., 2010, *AJ*, 139, 2097
- Peng C. Y., Impey C. D., Ho L. C., Barton E. J., Rix H., 2006, *ApJ*, 640, 114
- Peterson B. M., Ferrarese L., Gilbert K. M., Kaspi S., Malkan M. A., Maoz D., Merritt D., Netzer H., et al., 2004, *ApJ*, 613, 682
- Quillen A. C., Bower G. A., Stritzinger M., 2000, *ApJS*, 128, 85
- Rest A., van den Bosch F. C., Jaffe W., Tran H., Tsvetanov Z., Ford H. C., Davies J., Schafer J., 2001, *AJ*, 121, 2431
- Rix H., Carollo C. M., Freeman K., 1999, *ApJL*, 513, L25
- Sarzi M., Rix H., Shields J. C., Rudnick G., Ho L. C., McIntosh D. H., Filippenko A. V., Sargent W. L. W., 2001, *ApJ*, 550, 65
- Schlegel D. J., Finkbeiner D. P., Davis M., 1998, *ApJ*, 500, 525
- Scoville N. Z., Matthews K., Carico D. P., Sanders D. B., 1988, *ApJL*, 327, L61
- Seigar M. S., Graham A. W., Jerjen H., 2007, *MNRAS*, 378, 1575
- Sersic J. L., 1968, *Atlas de galaxias australes*
- Shen J., Gebhardt K., 2010, *ApJ*, 711, 484
- Shields G. A., Menezes K. L., Massart C. A., Vanden Bout P., 2006, *ApJ*, 641, 683
- Siopis C., Gebhardt K., Lauer T. R., Kormendy J., Pinkney J., Richstone D., Faber S. M., Tremaine S., et al., 2009, *ApJ*, 693, 946
- Soria R., Graham A. W., Fabbiano G., Baldi A., Elvis M., Jerjen H., Pellegrini S., Siemiginowska A., 2006, *ApJ*, 640, 143
- Tonry J. L., Dressler A., Blakeslee J. P., Ajhar E. A., Fletcher A. B., Luppino G. A., Metzger M. R., Moore C. B., 2001, *ApJ*, 546, 681
- Tremaine S., Gebhardt K., Bender R., Bower G. and Dressler A., Faber S. M., Filippenko A. V., Green R., et al., 2002, *ApJ*, 574, 740
- Treu T., Woo J., Malkan M. A., Blandford R. D., 2007, *ApJ*, 667, 117
- Trujillo I., Erwin P., Asensio Ramos A., Graham A. W., 2004, *AJ*, 127, 1917
- Valluri M., Merritt D., Emsellem E., 2004, *ApJ*, 602, 66
- van den Bosch F. C., Ferrarese L., Jaffe W., Ford H. C., O'Connell R. W., 1994, *AJ*, 108, 1579
- van der Marel R. P., van den Bosch F. C., 1998, *AJ*, 116, 2220
- Verolme E. K., Cappellari M., Copin Y., van der Marel R. P., Bacon R., Bureau M., Davies R. L., Miller B. M., de Zeeuw P. T., 2002, *MNRAS*, 335, 517
- Vika M., Driver S. P., Graham A. W., Liske J., 2009, *MNRAS*, 400, 1451
- Walsh J. L., Barth A. J., Ho L. C., Filippenko A. V., Rix H., Shields J. C., Sarzi M., Sargent W. L. W., 2008, *AJ*, 136, 1677
- Walter F., Carilli C., Bertoldi F., Menten K., Cox P., Lo K. Y., Fan X., Strauss M. A., 2004, *ApJL*, 615, L17
- Weinzirl T., Jogee S., Khochfar S., Burkert A., Kormendy J., 2009, *ApJ*, 696, 411
- Woo J.-H., Treu T., Malkan M. A., Blandford R. D., 2006, *ApJ*, 645, 900
- Zezas A., Birkinshaw M., Worrall D. M., Peters A., Fabbiano G., 2005, *ApJ*, 627, 711
- Zhao J.-H., Sumi D. M., Burns J. O., Duric N., 1993, *APJ*, 416, 51

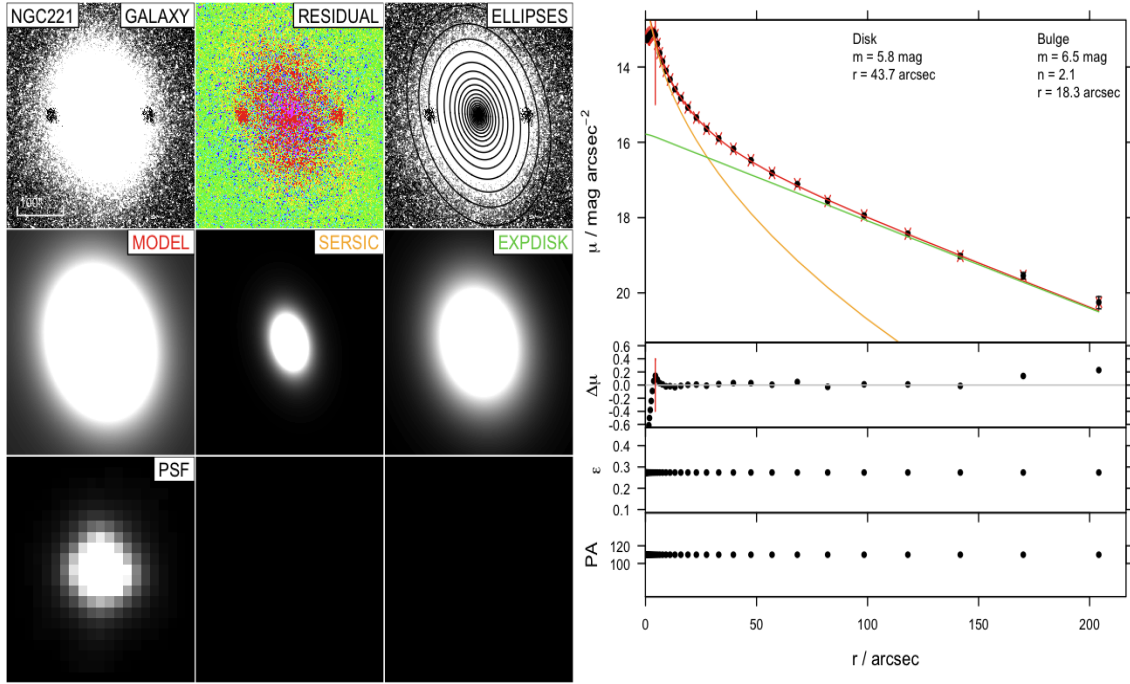


Figure 5. Two-dimension decomposition for NGC221. Left Panels: We display the original image, the residuals, the original image with IRAF ELLIPSE ellipses on top, the final model, the sub-components and the PSF which GALFIT3 used to convolve the original image. Right Panels from top to bottom: surface brightness μ , the deviation of the galaxy surface brightness (red line) from the model surface brightness, the ellipticity ϵ and the position angle PA of the bulge. The black circles indicate the surface brightness profiles of the original image while the red line the surface brightness from the model as ellipse measure them. The rest of the lines correspond to each of the sub-components. The colour of each line corresponds to the colour of the legend found on the left panel. The black line error bars show the uncertainty of estimating the surface brightness due to uncertainty of measuring the sky value. The red line error bars indicate the uncertainty of IRAF ELLIPSE to measure the surface brightness. The red vertical line indicate the use of a mask that prevents GALFIT3 from profiling the core of the galaxy. See the properties of the fitting components in Table 4.

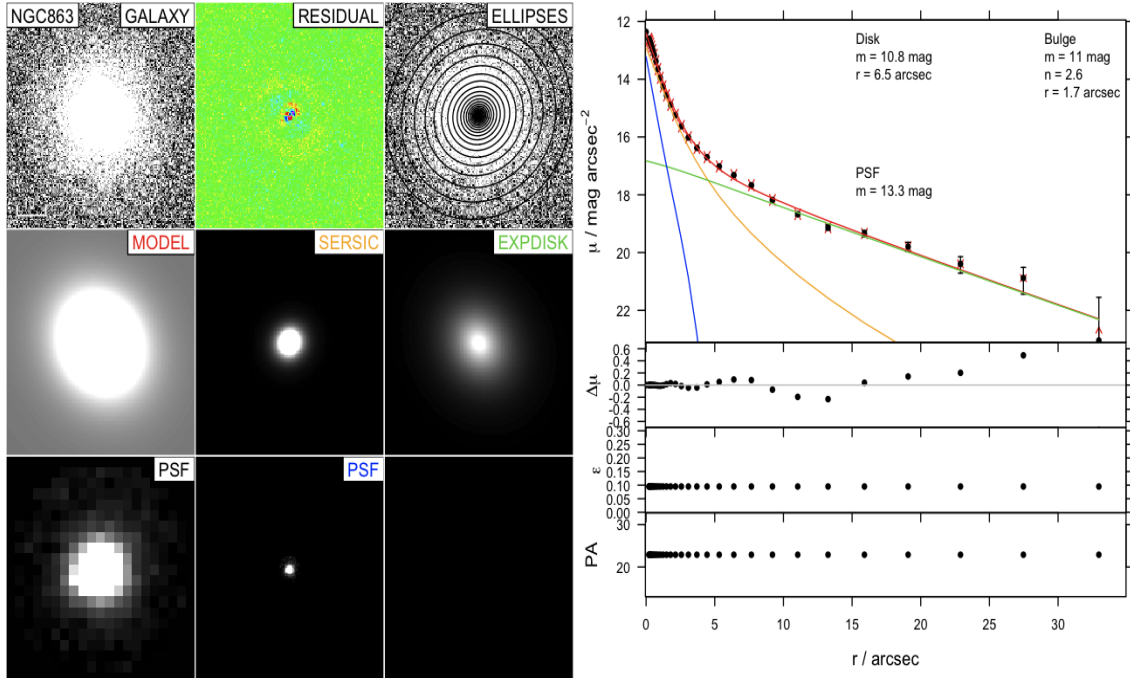


Figure 6. NGC863 has been classified as a spiral galaxy. The layout is as in Figure 5.

Table 4. GALFIT3 Derived Parameters. Column(1): name of the galaxy; Column(2-4): the spheroid apparent magnitude, effective radius along the semi-major axis and Sérsic index; Column (5-6): the disk apparent magnitude and scale-length; Column (7-9): the bar apparent magnitude, effective radius and Sérsic index; Column (10-11): the spheroid and total absolute magnitude; Column(12): the best fit chosen.

Galaxy Name (1)	m_{sph} (mag) (2)	r_{eff} (arcsec) (3)	n_{sph} Index (4)	m_{d} (mag) (5)	r_{s} (arcsec) (6)	m_{bar} (mag) (7)	r_{bar} (mag) (8)	n_{bar} Index (9)	M_{sph} (mag) (10)	M_{tot} (mag) (11)	best fit (12)
NGC221	6.5 ^{+0.88} _{-0.02}	18.3	2.1 ^{+0.01} _{-1.28}	5.8	43.7	/	/	/	-18.2	-19.5	bulge+disk+mask centre
NGC863	10.9 ^{+0.2} _{-0.32}	1.66	2.6 ^{+0.83} _{-0.001}	10.8	6.5	/	/	/	-18.4	-19.7	bulge+disk+psf
NGC1068	8.2 ^{+0.01} _{-0.08}	2.8	0.8 ^{+0.03} _{-0.02}	6.5	16.7	7.9	11.8	0.3	-22.7	-24.9	bulge+disk+bar+mask centre
NGC2778	10.9 ^{+0.96} _{-0.13}	1.5	2.7 ^{+0.04} _{-2.53}	10.7	5.4	/	/	/	-20.8	-21.9	bulge+disk
NGC2960	10.8 ^{+0.26} _{-0.09}	1.8	4.0 ^{+0.46} _{-0.98}	10.7	6.8	/	/	/	-23.5	-24.8	bulge+disk
NGC3245	9.0 ^{+0.2} _{-0.08}	3.5	2.6 ^{+0.14} _{-0.36}	8.3	20.5	/	/	/	-22.6	-24.1	bulge+disk
NGC4258	7.8 ^{+0.17} _{-0.08}	17.0	3.5 ^{+0.34} _{-0.11}	6.7	50.2	/	/	/	-21.5	-24	bulge+disk+psf
NGC4261	7.3 ^{+0.06} _{-0.1}	24.2	3.5 ^{+0.19} _{-0.27}	/	/	/	/	/	-25.2	-25.2	elliptical+mask centre
NGC4303	9.5 ^{+0.03} _{-0.01}	2.8	0.9 ^{+0.01} _{-0.05}	7.5	30.0	9.1	49.5	0.5	-21.6	-25.2	bulge+disk+bar+psf
NGC4342	10.3 ^{+0.008} _{-0.004}	0.86	1.9 ^{+0.02} _{-0.001}	9.6	5.1	/	/	/	-20.9	-22.3	bulge+disk
NGC4374	6.4 ^{+0.02} _{-0.01}	28.7	3.5 ^{+0.02} _{-0.03}	/	/	/	/	/	-24.9	-24.9	elliptical+mask centre
NGC4435	8.8 ^{+0.03} _{-0.08}	4.5	1.5 ^{+0.05} _{-0.05}	8.7	18.9	9.9	20.8	0.3	-22	-22.9	bulge+disk+bar
NGC4459	7.2 ^{+0.11} _{-0.11}	25.0	3.9 ^{+0.54} _{-0.33}	/	/	/	/	/	-23.8	-24.1	elliptical+moffat core
NGC4473	7.2 ^{+0.11} _{-0.07}	21.3	4.3 ^{+0.43} _{-0.45}	/	/	/	/	/	-23.7	-23.7	elliptical+mask centre
NGC4486	6.0 ^{+0.45} _{-0.2}	34.6	2.4 ^{+0.54} _{-1.68}	/	/	/	/	/	-25.0	-25.0	elliptical+mask centre
NGC4486a	9.3 ^{+0.12} _{-0.14}	8.1	2.0 ^{+0.28} _{-0.72}	/	/	/	/	/	-21.9	-21.9	elliptical+mask centre
NGC4486b	10.0 ^{+0.12} _{-0.13}	2.6	3.2 ^{+0.12} _{-0.31}	/	/	/	/	/	-21.2	-21.2	elliptical
NGC4552	6.9 ^{+0.05} _{-0.11}	16.7	3.6 ^{+0.31} _{-0.33}	/	/	/	/	/	-24.0	-24.0	elliptical
NGC4564	9.4 ^{+0.06} _{-0.01}	3.0	3.7 ^{+0.1} _{-0.24}	/	/	8.6	23.4	1.3	-21.4	-23.1	bulge+disk
NGC4596	8.3 ^{+0.14} _{-0.05}	13.2	3.6 ^{+0.08} _{-0.25}	8.6	44.7	9.1	37.9	0.4	-22.9	-24	bulge+disk+bar
NGC4621	6.5 ^{+0.09} _{-0.1}	54.7	5.7 ^{+0.22} _{-0.41}	/	/	/	/	/	-24.8	-24.8	elliptical+mask centre
NGC4649	5.7 ^{+0.19} _{-0.14}	45.7	3.6 ^{+0.54} _{-0.75}	/	/	/	/	/	-25.4	-25.4	elliptical+mask centre
NGC4697	6.6 ^{+0.01} _{-0.03}	39.1	3.8 ^{+0.03} _{-0.01}	/	/	/	/	/	-20.3	-20.3	elliptical
NGC5576	7.8 ^{+0.24} _{-0.17}	16.9	5.1 ^{+1.06} _{-1.94}	/	/	/	/	/	-24.2	-24.3	elliptical+mask centre
NGC5813	6.7 ^{+0.66} _{-0.65}	132.9	8.3 ^{+2.55} _{-2.69}	/	/	/	/	/	-25.9	-25.9	elliptical+mask centre
NGC5845	9.2 ^{+0.01} _{-0.02}	3.5	2.6 ^{+0.07} _{-0.06}	/	/	/	/	/	-22.8	-22.9	elliptical
NGC5846	6.8 ^{+1.07} _{-0.33}	46.3	3.7 ^{+1.07} _{-5.29}	/	/	/	/	/	-25.2	-25.1	elliptical+mask centre
NGC7052	10.0 ^{+0.03} _{-0.07}	4.3	1.8 ^{+0.08} _{-0.01}	9.2	15.2	/	/	/	-24.2	-25.6	bulge+disk
UGC9799	9.4 ^{+0.48} _{-0.26}	31.3	2.9 ^{+0.41} _{-0.96}	/	/	/	/	/	-26.4	-26.8	elliptical+mask centre

Table 5. Second better fit chosen. The layout is as in Table 4.

Galaxy Name (1)	m_{sph} (mag) (2)	r_{eff} (arcsec) (3)	n_{sph} Index (4)	m_{d} (mag) (5)	r_{s} (arcsec) (6)	m_{bar} (mag) (7)	r_{bar} (mag) (8)	n_{bar} Index (9)	M_{sph} (mag) (10)	M_{tot} (mag) (11)	best fit (12)
NGC4258	8.8 ^{+0.2} _{-0.09}	6.3	2.2 ^{+0.4} _{-0.12}	6.6	50.0	8.9	0.9	22.0	-20.5	-24	bulge+disk+bar+psf
NGC4374	7.6 ^{+0.04} _{-0.03}	7.8	1.6 ^{+0.02} _{-0.04}	7.0	22.8	/	/	/	-23.7	-24.9	bulge+disk
NGC4435	8.8 ^{+0.02} _{-0.07}	4.5	1.5 ^{+0.04} _{-0.03}	8.6	17.4	9.8	0.4	19.9	-21.9	-22.9	bulge+disk+bar+psf
NGC4486b	11.2 ^{+0.11} _{-0.11}	0.9	1.8 ^{+0.15} _{-0.11}	10.7	2.2	/	/	/	-20.0	-21.2	bulge+disk
NGC4697	7.9 ^{+0.01} _{-0.03}	10.0	2.9 ^{+0.03} _{-0.01}	7.2	23.8	/	/	/	-22.4	-20.3	bulge+disk
NGC7052	8.6 ^{+0.04} _{-0.06}	18.8	3.5 ^{+0.05} _{-0.01}	/	/	/	/	/	-25.6	-25.6	elliptical+mask centre

Table 6. Galaxy Sample; Column(2): The distances have come from Tonry et al. (2001) unless otherwise specified. Column(3): The black hole masses have been adjusted to the distance given in column 2. Column(4): The method of measuring the black hole mass: s-stellar kinematics, g-gas kinematics, m-water masers, p-stellar proper motion and r-reverberation mapping. Column(5-6): Sérsic indices and their band. References: (1)Verolme et al. 2002; (2)Peterson et al. 2004; (3)Lodato & Bertin 2003; (4)Gebhardt et al. 2003; (5)Henkel et al. 2002; (6)Barth et al. 2001; (7)Herrnstein et al. 1999; (9)Siopis et al. 2009; (10)Ferrarese et al. 1996; (11)Pastorini et al. 2007; (12)Jerjen et al. 2004; (13)Cretton & van den Bosch 1999; (14)Maciejewski & Binney 2001; (15)Coccatto et al. 2006; (16)Sarzi et al. 2001; (17)Macchetto et al. 1997; (18) Ferrarese et al. 1996; (19)Nowak et al. 2007; (20)Valluri et al. 2004; (21)Kormendy et al. 1997; (22) Cappellari et al. 2008; (23)Dalla Bontà et al. 2009 ; (24)NED/Virgo + GA + Shapley corrected Hubble flow distances; (25)van der Marel & van den Bosch 1998 ; (26)Graham & Driver 2007 ; (27)Kormendy et al. 2009; (28)Seigar et al. 2007; (29)Gültekin et al. 2009; (30)Gebhardt & Thomas 2009; (31)Shen & Gebhardt 2010.

Galaxy Name (1)	Distance (Mpc) (2)	M_{bh} ($10^8 M_{\odot}$) (3)	method-ref (4)	n_{sph} (mag) (5)	Band-ref (6)
NGC221	0.86	$0.025^{+0.005}_{-0.005}$	s-1	1.32	R-26
NGC863	7.4 (24)	$0.47^{+0.074}_{-0.074}$	r-2	/	/
NGC1068	15.2 (24)	$0.084^{+0.003}_{-0.003}$	m-3	/	/
NGC2778	22.3	$0.15^{+0.09}_{-0.10}$	s-4	1.60	R-26
NGC2960	72.8 (24)	$0.12^{+0.03}_{-0.03}$	m-5	/	/
NGC3245	20.9	$2.1^{+0.5}_{-0.5}$	g-6	/	/
NGC4258	7.2 (7)	$0.3^{+0.2}_{-0.2}$	s-9	2.04	R-26
NGC4261	31.6	$5.2^{+1.0}_{-1.1}$	g-10	7.30	R-26
NGC4303	16.1 (18)	0.006-0.16	g-11	/	/
NGC4342	17.0 (12)	$3.3^{+1.9}_{-1.1}$	s-13,20	/	/
NGC4374	18.4	$4.64^{+3.46}_{-1.83}$	g-14	5.60	V-27
NGC4435	14.0(24)	<0.075	g-15	/	/
NGC4459	16.1	$0.70^{+0.13}_{-0.13}$	g-16	3.17	V-27
NGC4473	15.3	$1.2^{+0.4}_{-0.9}$	s-4	2.73	R-26
NGC4486	16.1	34^{+10}_{-10}	g-17	11.84	V-27
NGC4486a	17.0 (12)	$0.13^{+0.08}_{-0.08}$	s-19	2.04	V-27
NGC4486b	17.0 (12)	$6.0^{+3.0}_{-2.0}$	s-21	2.2	V-27
NGC4552	15.3	$4.8^{+0.8}_{-0.8}$	s-22	9.22	V-27
NGC4564	14.6	$0.60^{+0.03}_{-0.09}$	s-4	3.15	R-26
NGC4596	17.0 (18)	$0.79^{+0.38}_{-0.33}$	g-16	/	/
NGC4621	18.3	$4.0^{+0.6}_{-0.6}$	s-22	5.36	V-27
NGC4649	16.8	$22.0^{+4.0}_{-6.0}$	s-4	6.04	R-26
NGC4697	11.4	$1.8^{+0.2}_{-0.1}$	s-4	4.00	R-26
NGC5576	24.8	$1.8^{+0.3}_{-0.4}$	s-29	/	/
NGC5813	32.2	$7.0^{+1.1}_{-1.1}$	s-22	/	/
NGC5845	25.2	$2.6^{+0.4}_{-1.5}$	s-4	3.22	R-26
NGC5846	24.9	$11.0^{+2.0}_{-2.0}$	s-22	/	/
NGC7052	66.4 (24)	$3.7^{+2.6}_{-1.5}$	g-25	4.55	R-26
UGC9799	141 (23)	<46.0	g-23	1.4	R-28

Table 7. Galaxy Sample - Additional SMBH mass - galaxy distance measurements. The layout is as in Table 6.

Galaxy Name (1)	Distance (Mpc) (2)	M_{bh} ($10^8 M_{\odot}$) (3)	method-ref (4)
NGC4486	17.9	64^{+5}_{-5}	s-30
NGC4649	15.7	45^{+10}_{-10}	s-31

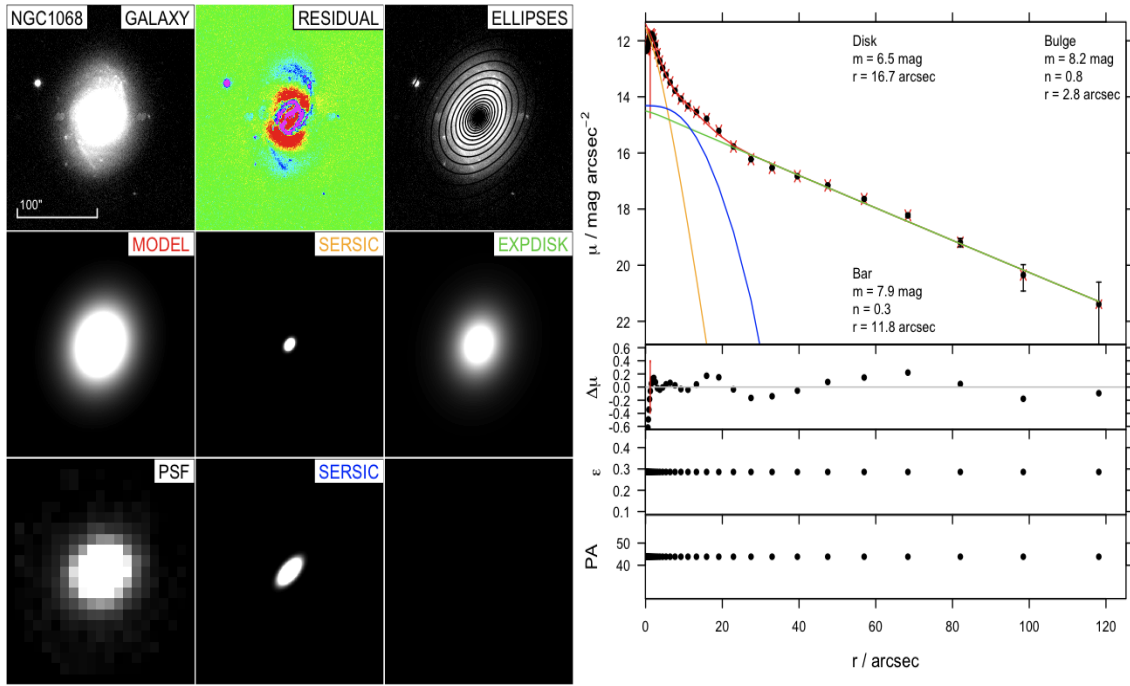


Figure 7. At the nuclei of the galaxy arise an artificial drop of counts. To prevent GALFIT3 profiling this inner part we masked the nuclei with a box of 1.5 arcsec². The layout is as in Figure 5.

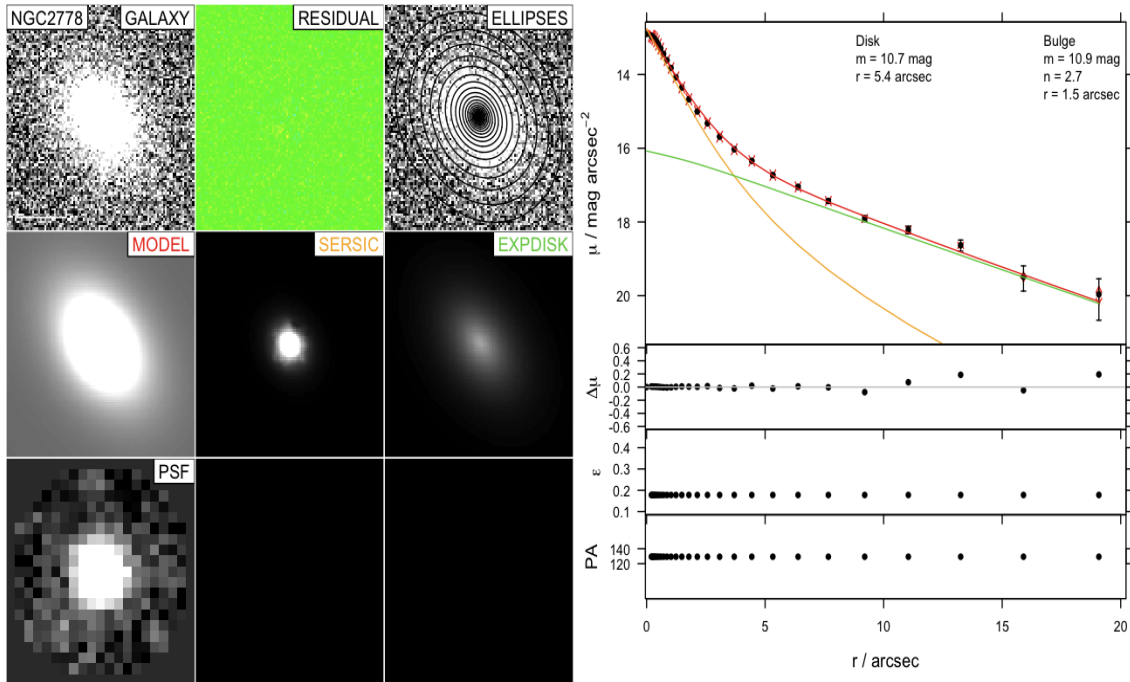


Figure 8. The surface brightness profile for NGC2778. The layout is as in Figure 5.

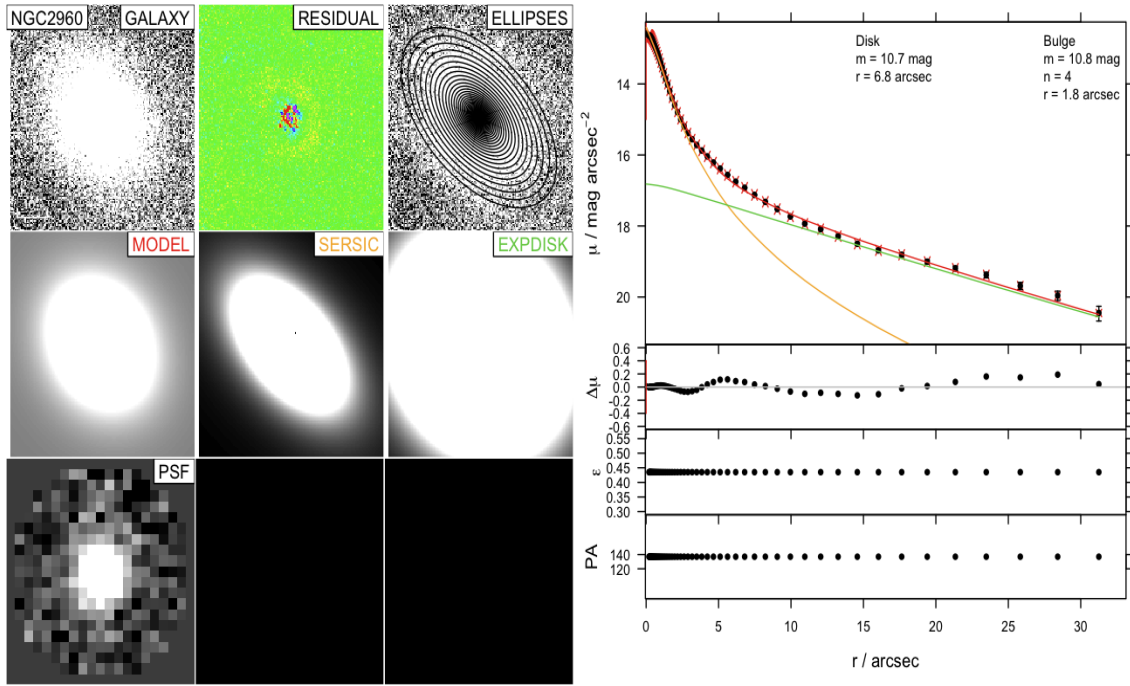


Figure 9. The location of the galaxy on the image does not permit GALFIT3 to profile the galaxy further than 35 arcsec. But even under this limitation GALFIT3 output look to be realistic so we trust the bulge properties. The layout is as in Figure 5.

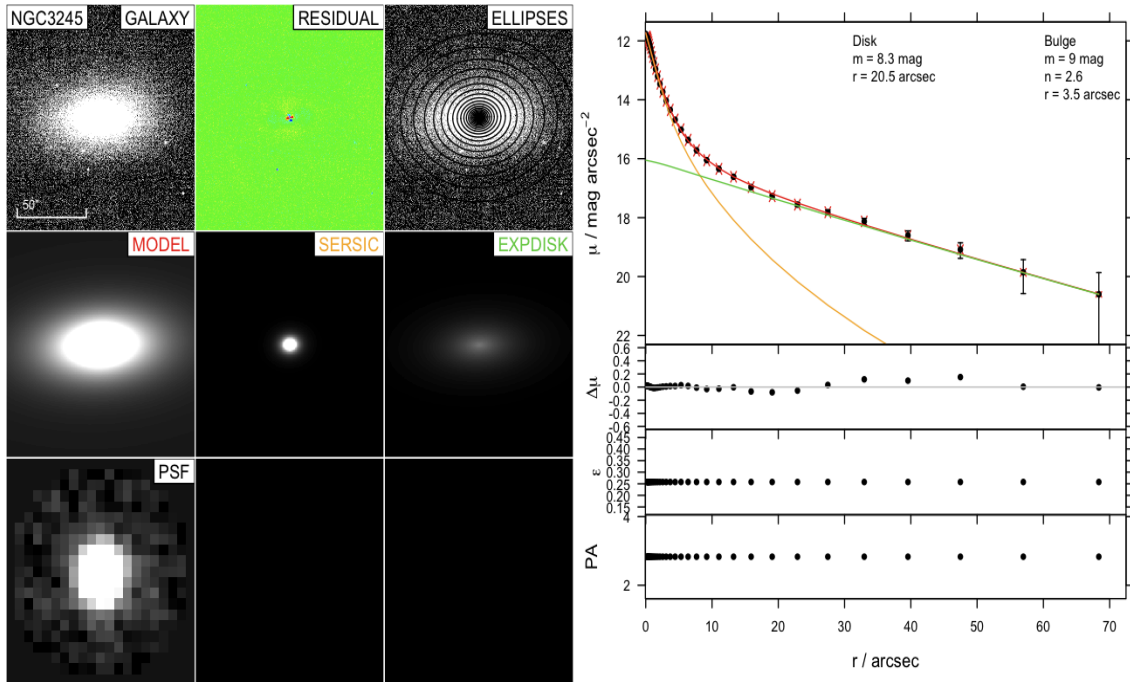


Figure 10. GALFIT3 results are in agreement with the kinematics studies that show existence of disk. The layout is as in figure 5.

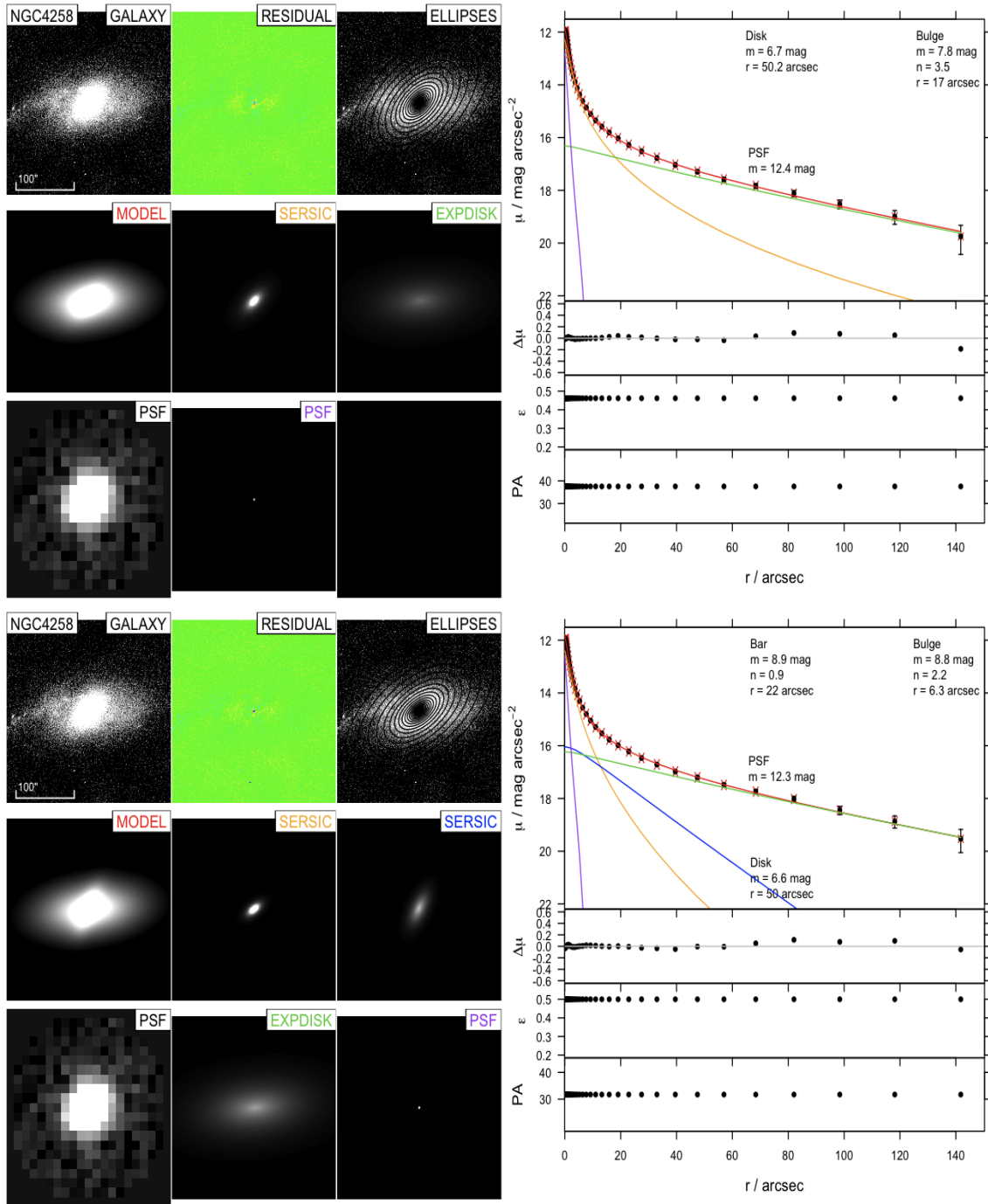


Figure 11. The surface brightness profile for NGC4258 for two different fits: (a) Sérsic + exponential model + PSF nuclei and (b) double Sérsic + exponential model + PSF nuclei. The layout is as in Figure 5.

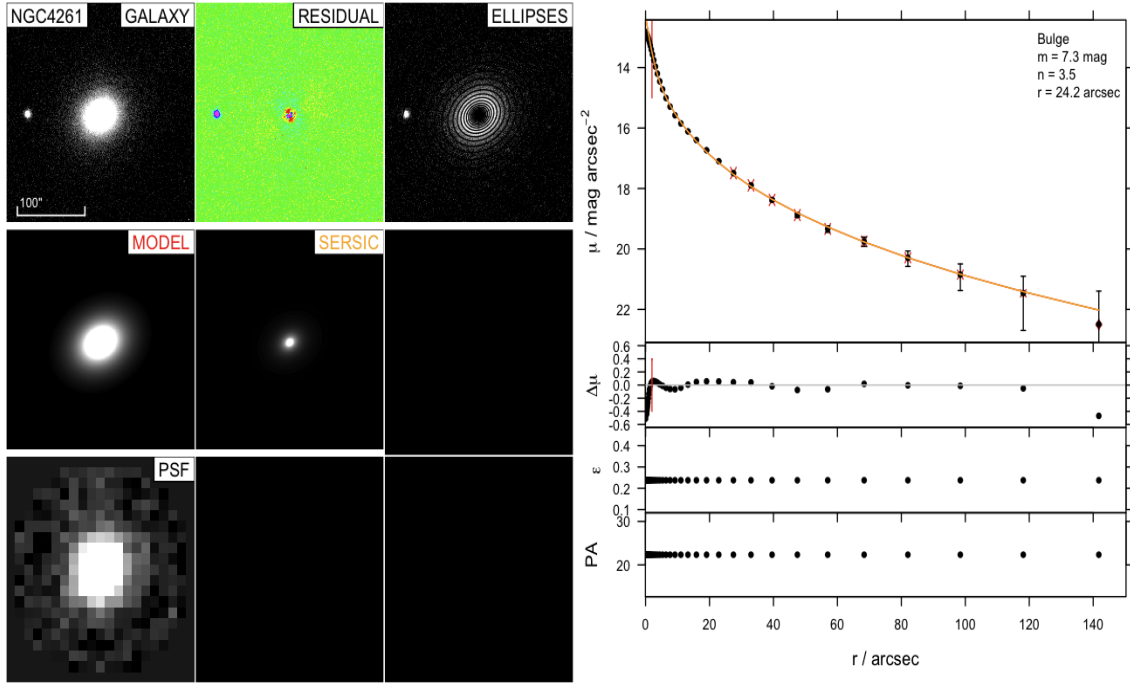


Figure 12. For the NGC4261 galaxy GALFIT3 generate low Sérsic index model compared to the one dimensional pre-existing models (see Subsection 3.2). We masked the inner 2 arcsec. The layout is as in Figure 5.

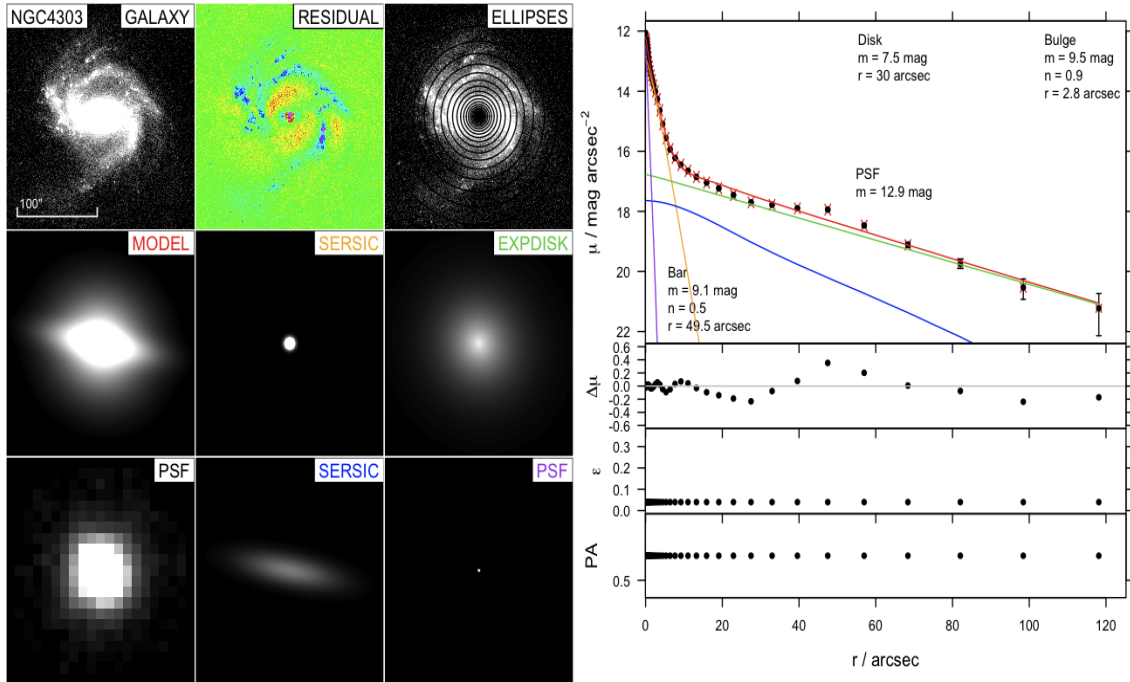


Figure 13. The surface brightness profile for NGC4303. The layout is as in Figure 5.

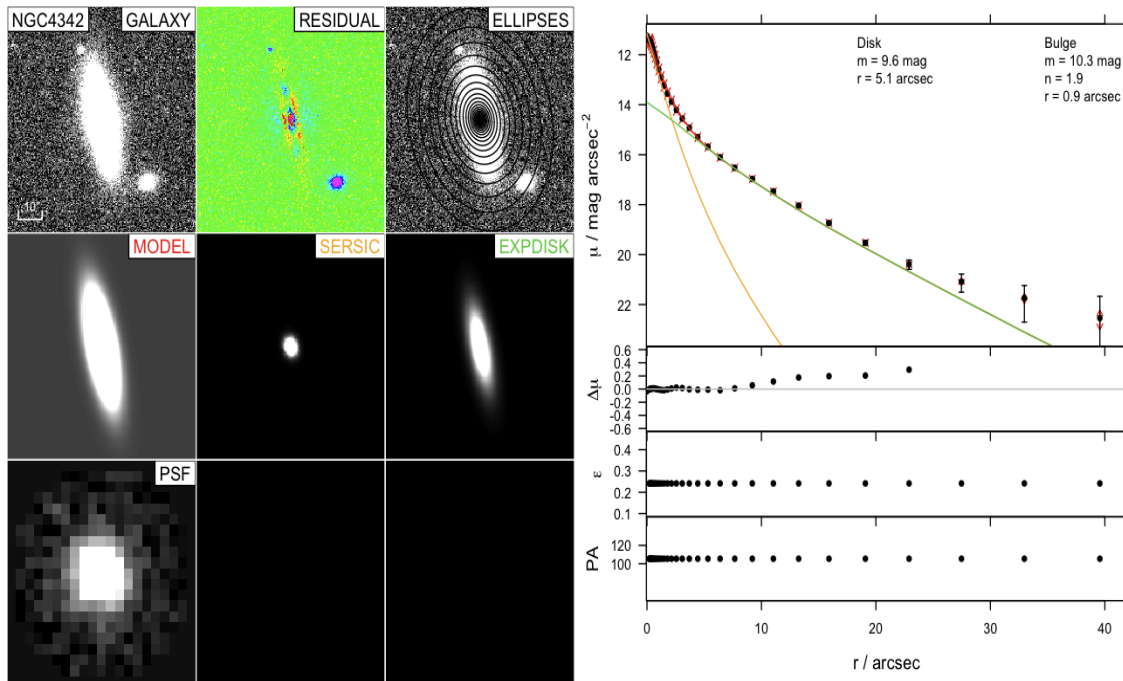


Figure 14. The layout is as in Figure 5. IRAF ELLIPSE outer ellipses are contaminated with extra light from the satellites as a result the model surface brightness mismatch IRAF ELLIPSE points.

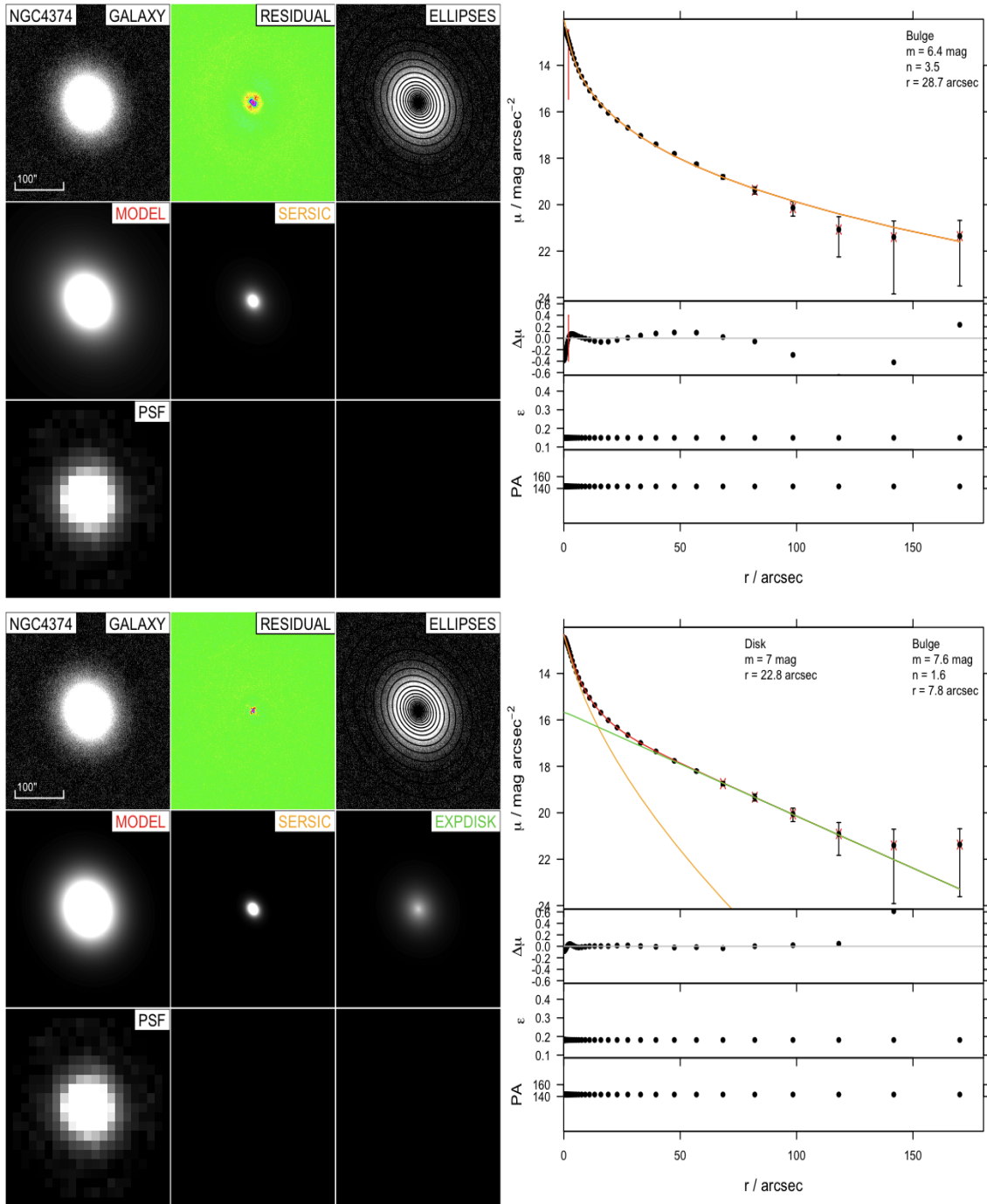


Figure 15. NGC4374 has been classified as an high Sérsic index elliptical galaxy from previous studies. We believe that NGC4374 can also be profiled with a two components model. The layout is as in Figure 5.

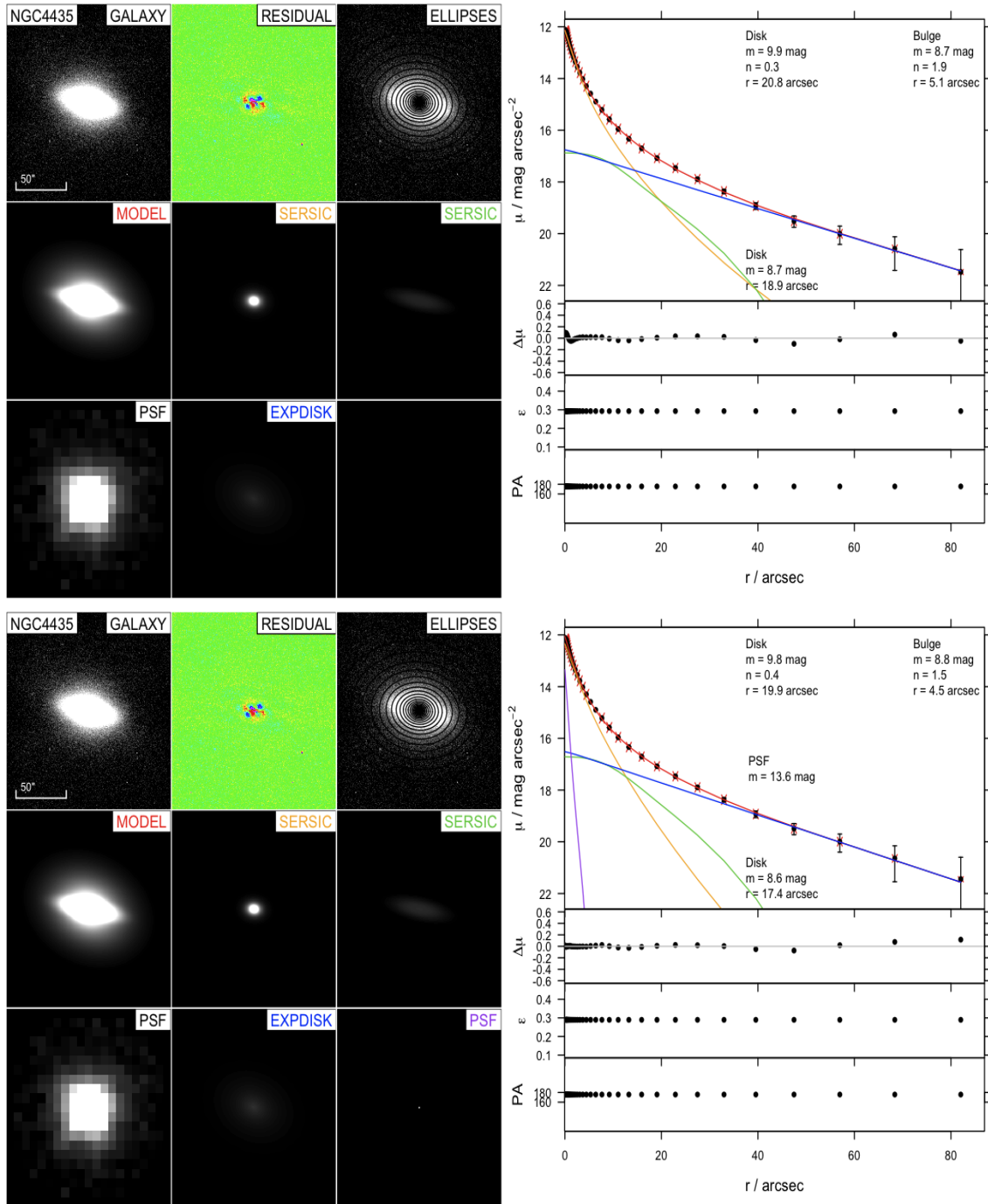


Figure 16. The surface brightness profile for NGC4435 for different fits: (a) double Sérsic + exponential model and (b) double Sérsic + exponential model + PSF nuclei. The layout is as in Figure 5.

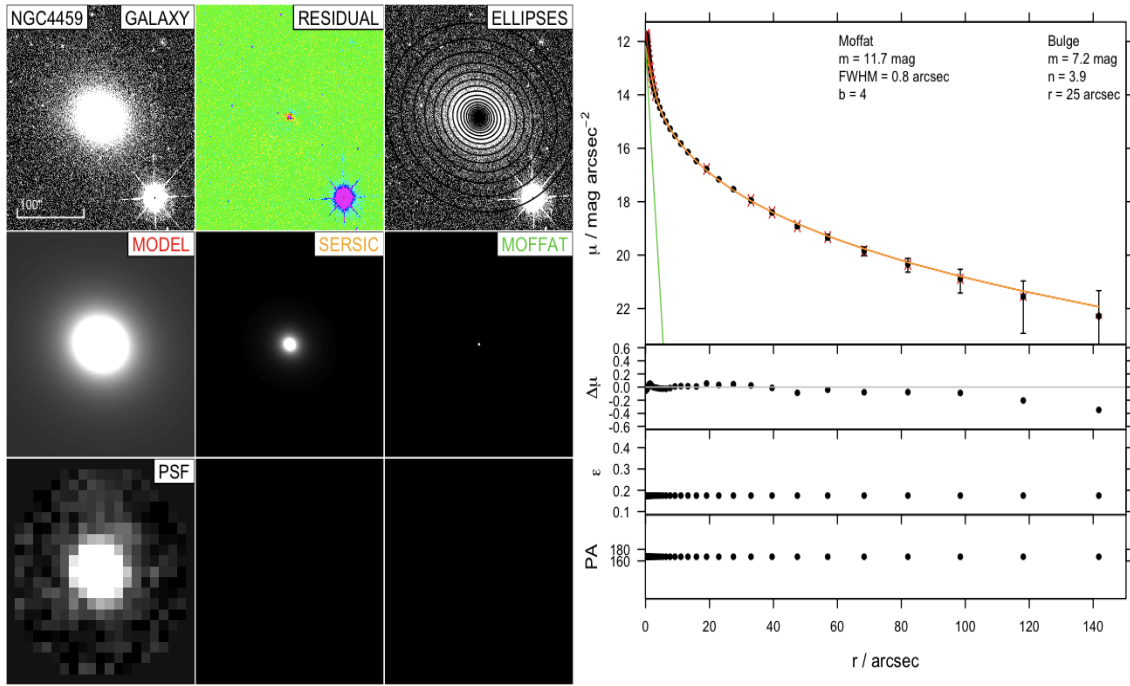


Figure 17. NGC4459 has been classified as an S0 or as an elliptical galaxy from different studies. Our profiles show that is an elliptical galaxy with an extra light in the center that need to be mask or profiled. We found that the function that describes better this core light is the Moffat function. For more details about how we apply the Moffat function see Section 3. The layout is as in Figure 5.

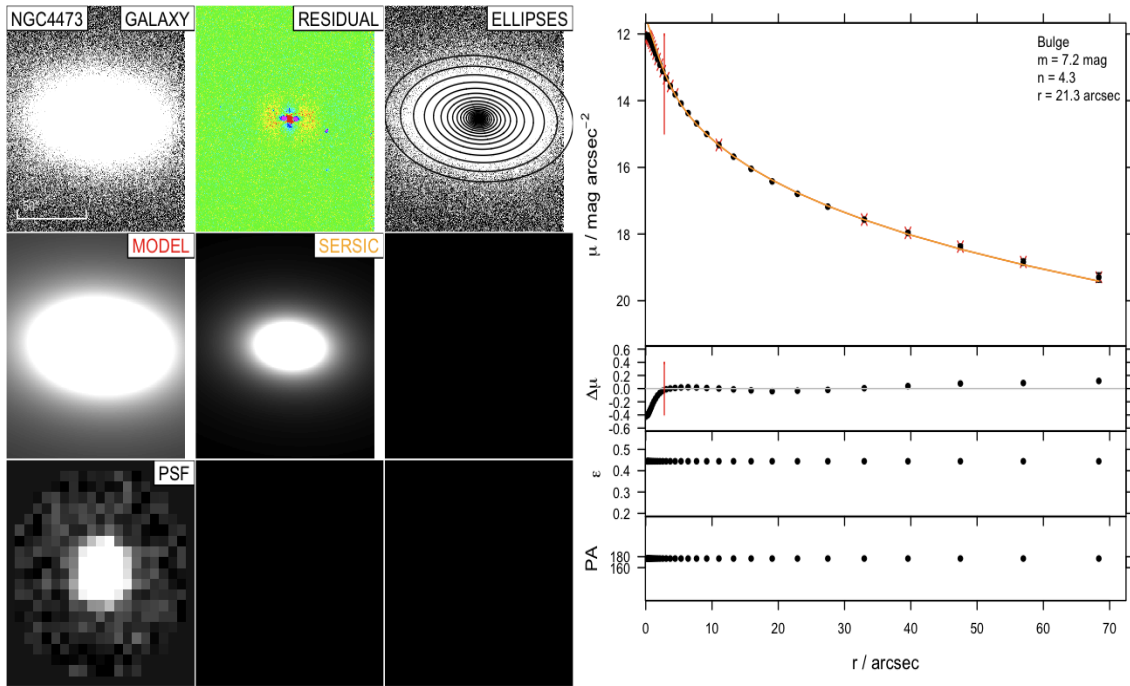


Figure 18. NGC4473 has been classified as an elliptical galaxy with an inner rotating disk. We masked the inner 2.8 arcsec. The layout is as in Figure 5.

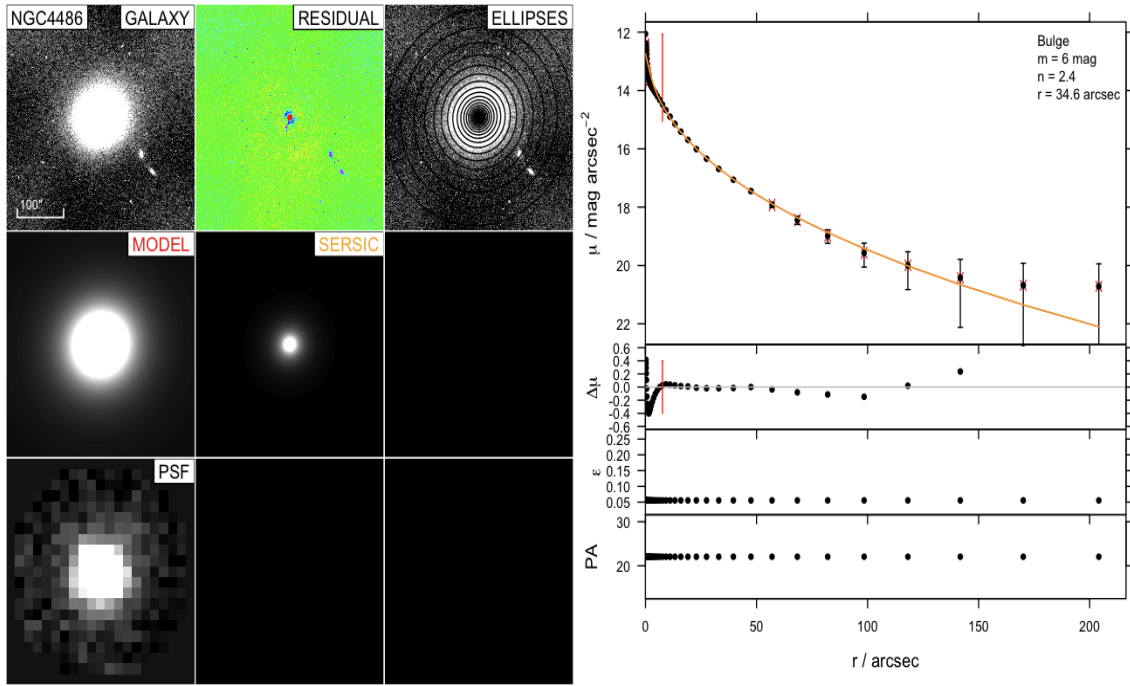


Figure 19. M87 is an elliptical galaxy with a recognisable jet in most of the wavelengths. We masked the inner 7.5 arcsec. Notice the Sérsic index variance between one dimensional and two dimensional profiles (see Section 3.2). The layout is as in Figure 5.

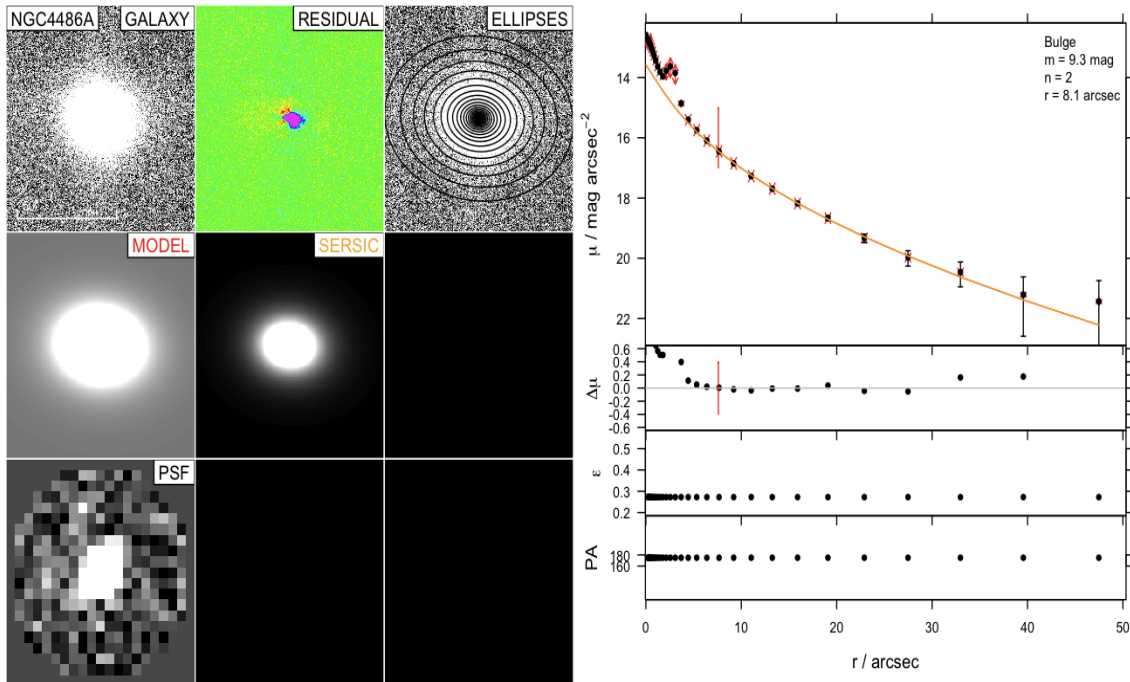


Figure 20. For profiling NGC4486A we masked the inner 7 arcsec where the flux is contaminated by a star placed next to the core of the galaxy. The layout is as in Figure 5.

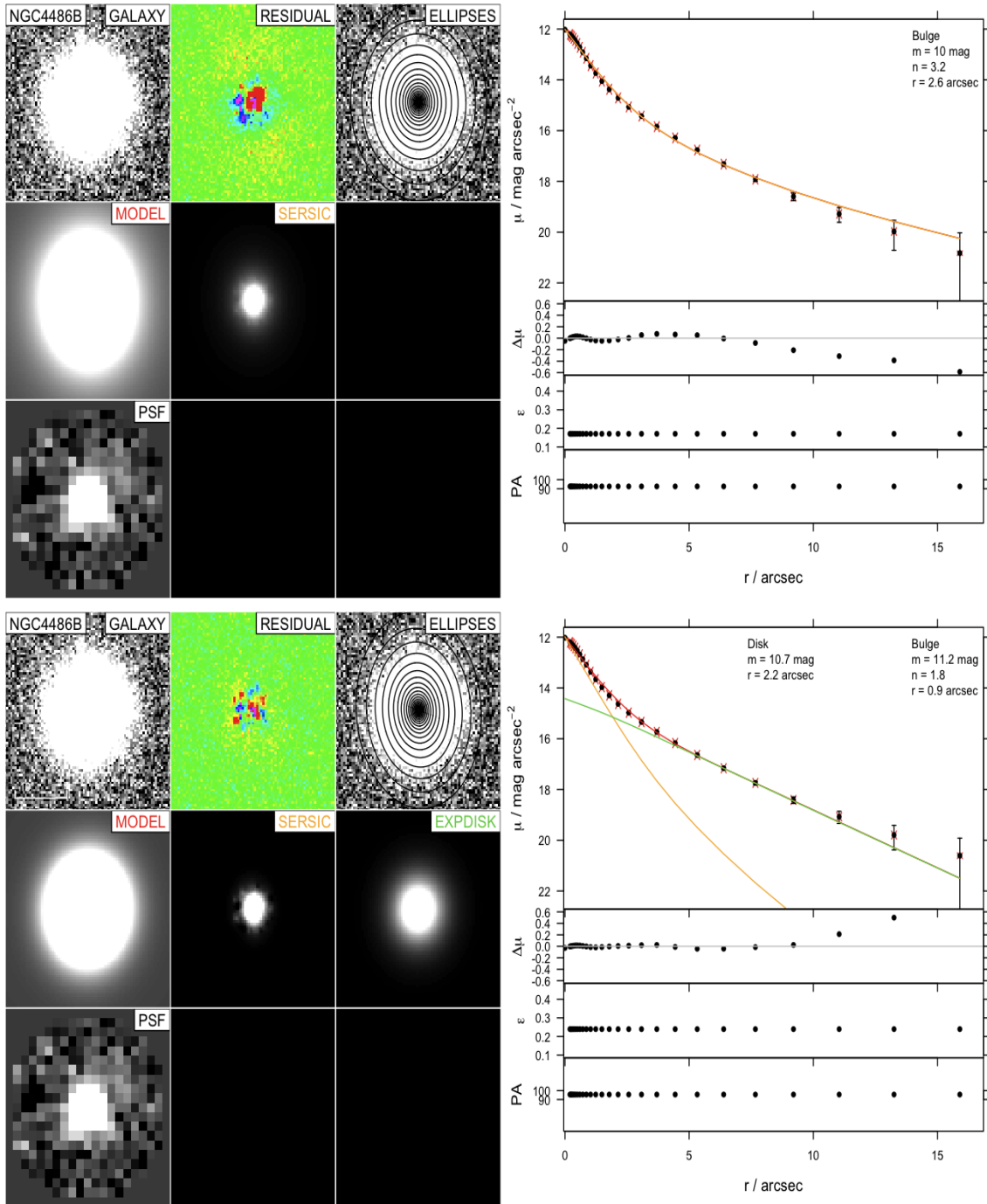


Figure 21. NGC4486B has been characterised as a low luminosity cE0 with extra light in the center. Our surface brightness profile for NGC4486B for two different fits: (a) single Sérsic and (b) Sérsic + exponential. The layout is as in Figure 5.

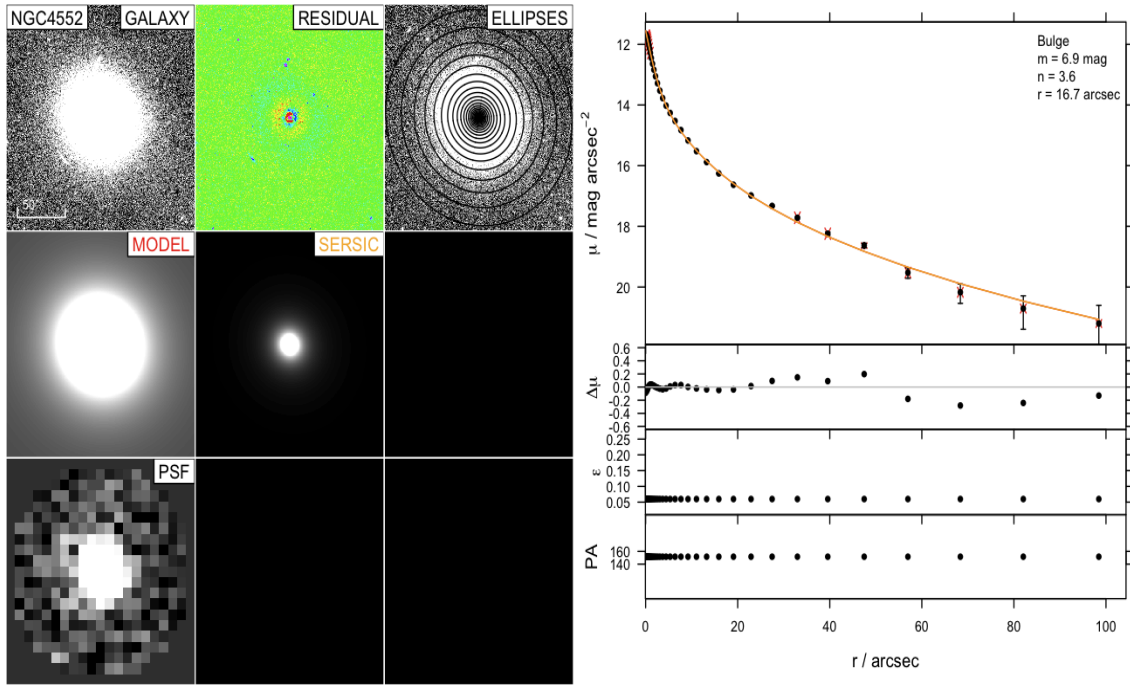


Figure 22. Notice the Sérsic index variance between one dimensional and two dimensional profiles (see Section 3.2). The layout is as in Figure 5.

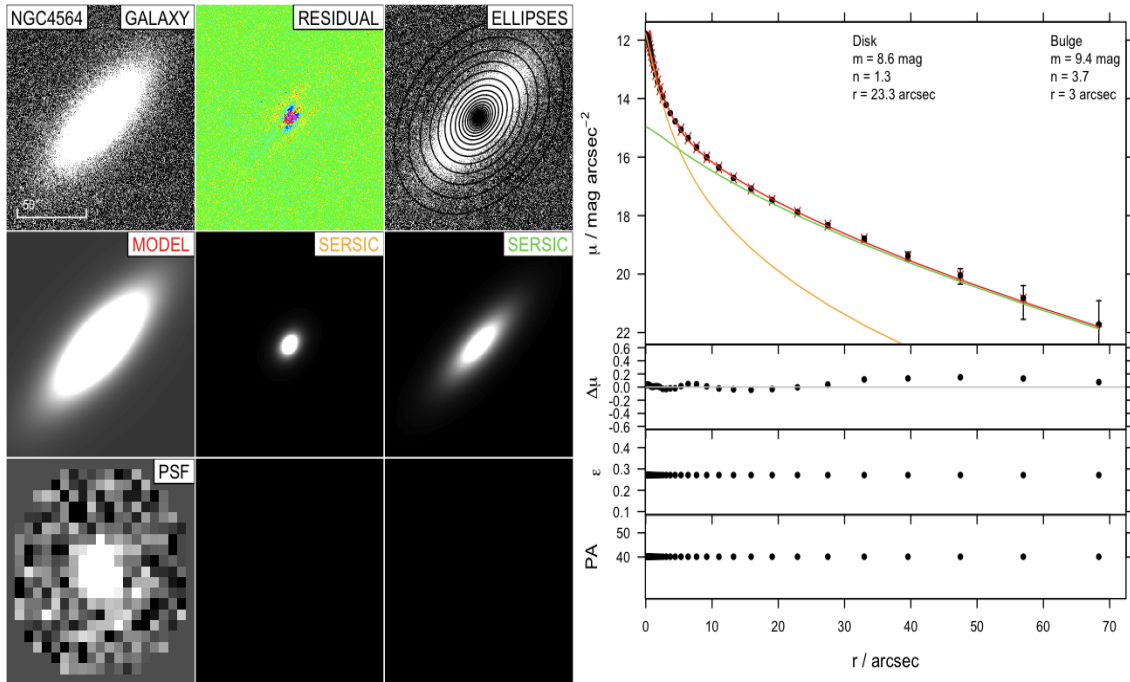


Figure 23. The NGC4564 best fit is with a double Sérsic model. The layout is as in Figure 5.

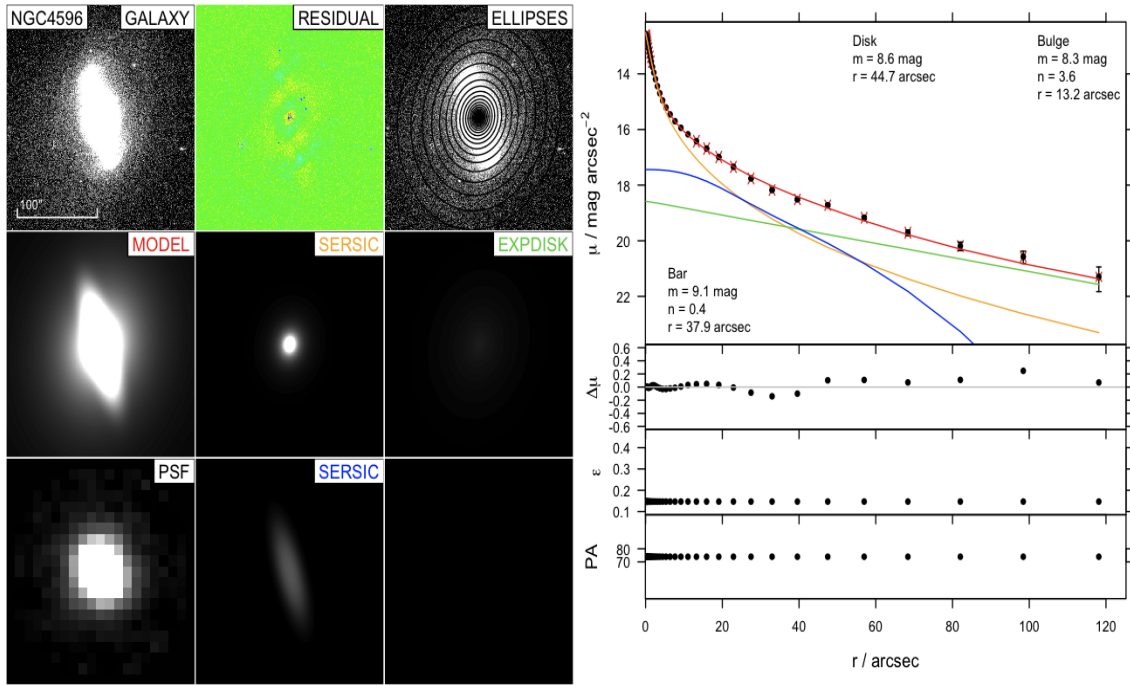


Figure 24. The surface brightness profile for NGC4596. The layout is as in Figure 5.

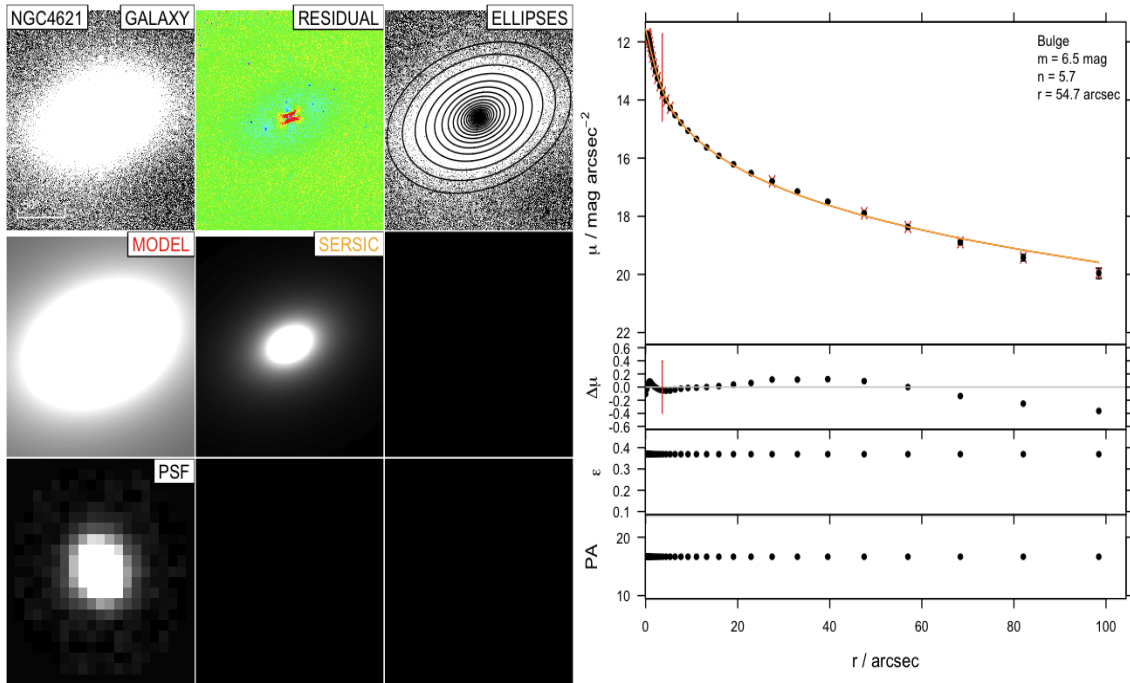


Figure 25. NGC4621 has been classified as an S0 and as an elliptical galaxy from different studies. We do not find evidences of a disk but the existence of a core which we masked (3.6 arcsec). The layout is as in Figure 5.

APPENDIX A: GALFIT3 SIGMA MAP

In this paper we profiled a sample of 29 galaxies by allowing **GALFIT3** to create the sigma (weight) maps internally. In this Section we want to repeat the fit for the full sample by providing an external sigma map for each galaxy. The construction of the external maps is based on the same formulae that **GALFIT3** uses internally:

$$\sigma^{[ADU]}(x, y) = \frac{\sqrt{\sigma_d^{[e^-]}(x, y)^2 + \sigma_{sky}^{[e^-]}(x, y)^2}}{gain} \quad (A1)$$

$$= \sqrt{\frac{f_d^{[ADU]}(x, y) - sky^{[ADU]}}{gain} + \sigma_{sky}^{[ADU]}(x, y)^2} \quad (A2)$$

where

$$\sigma_d^{[e^-]}(x, y) = \sqrt{(f_d^{[ADU]}(x, y) - sky^{[ADU]})gain} \quad (A3)$$

where $f_d(x, y)$ is the image flux at pixel (x,y) in *ADU* units, *sky* is the sky value listed in Table 2, *gain* is equal to $4.5 e^- ADU$, and $\sigma_{sky}(x, y)$ is the full resolution noise map of the sky background created by **SExtractor**. The sigma map shows the flux uncertainty at each pixel and the construction is based on Poisson statistics. The created sigma map is compatible with **GALFIT3** and can replace the internal sigma map.

After the sigma map has been created we re-run **GALFIT3** using as input/starting values the best fit values found in Table 4 but instead of permitting an internal weight map estimation we provide the external weight map. Figure A1 shows that there is no significant change in using a **GALFIT3** internal sigma map or a **SExtractor** external sigma map.

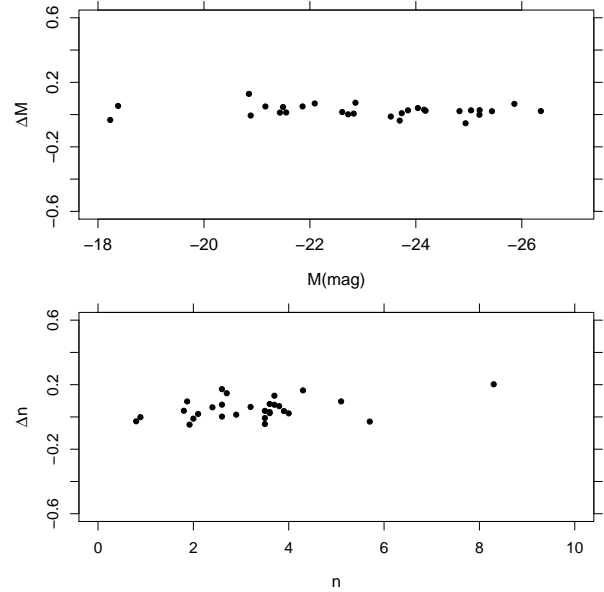


Figure A1. Top panel: A plot of the **GALFIT3** magnitude differences found using either an internal sigma map or an external sigma map against the range of internal magnitudes. Bottom panel: The same for the Sérsic index.

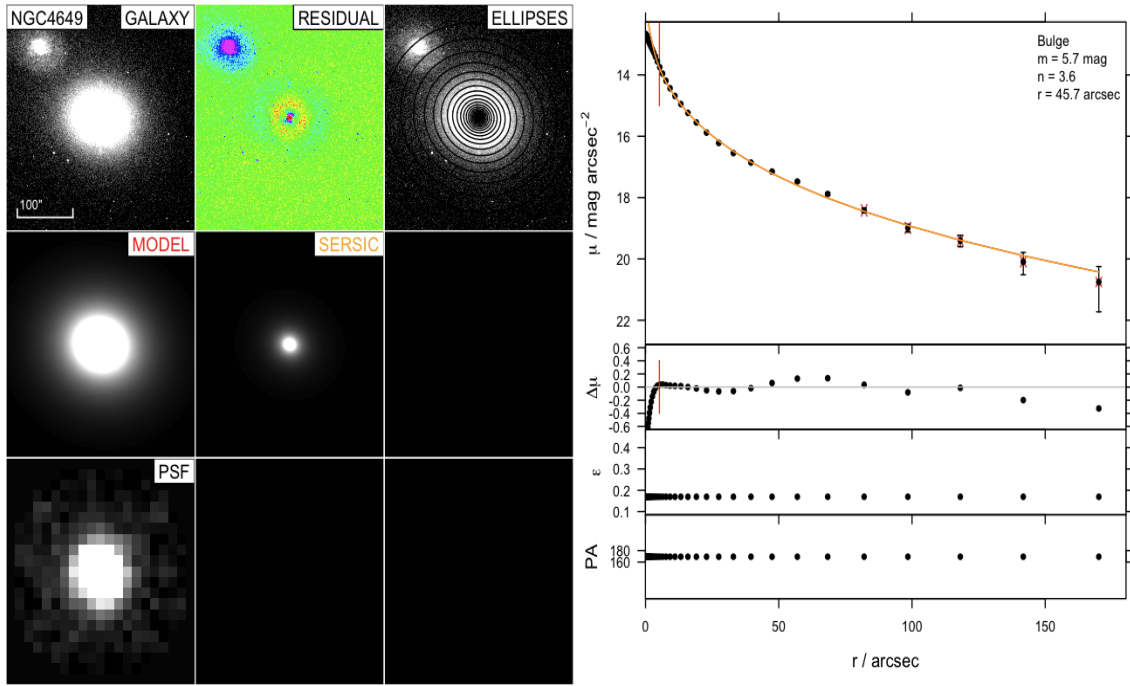


Figure 26. The surface brightness profile for NGC4649, we masked the inner 5.2 arcsec. The layout is as in Figure 5.

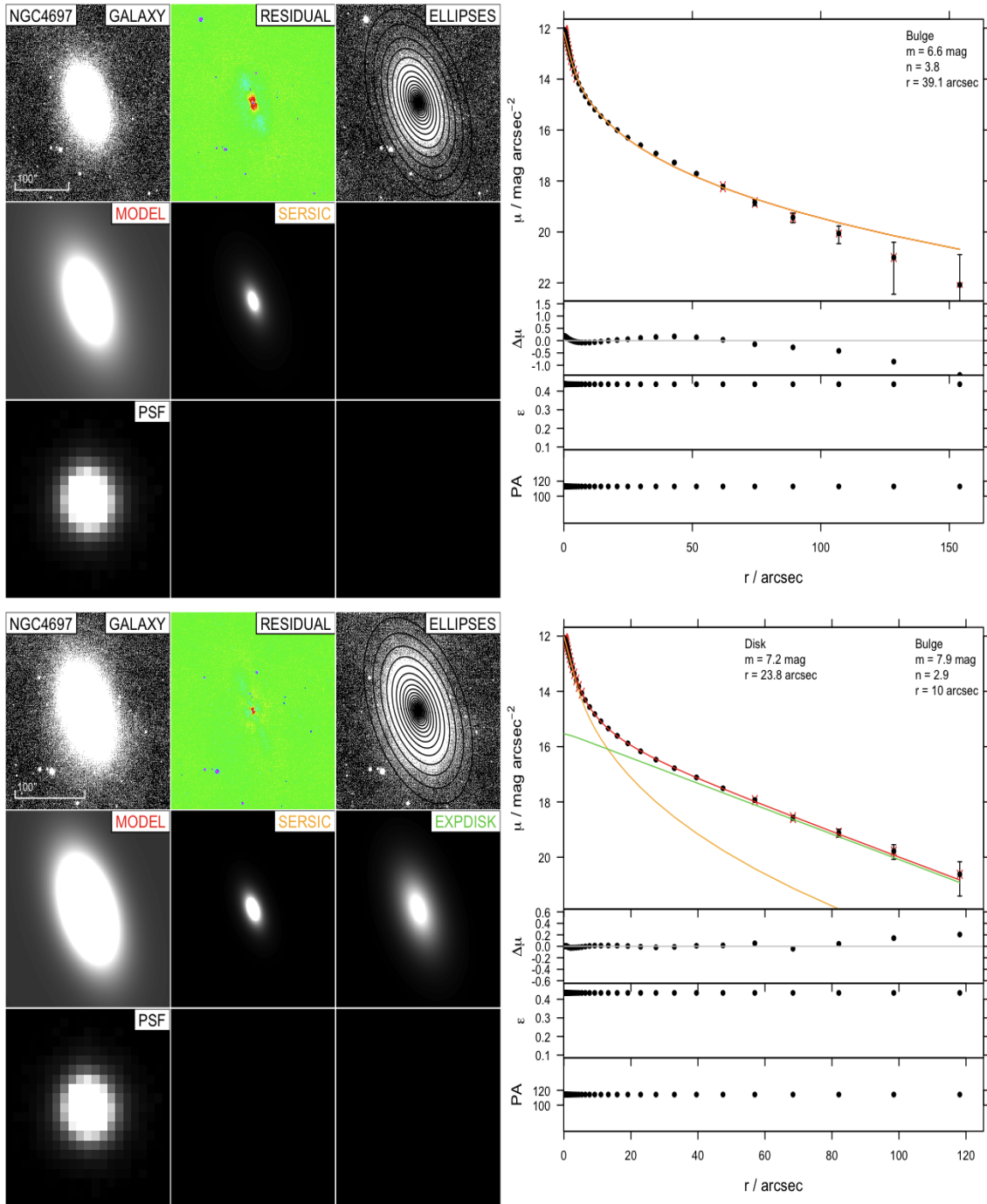


Figure 27. The surface brightness profile for NGC4697. The layout is as in Figure 5.

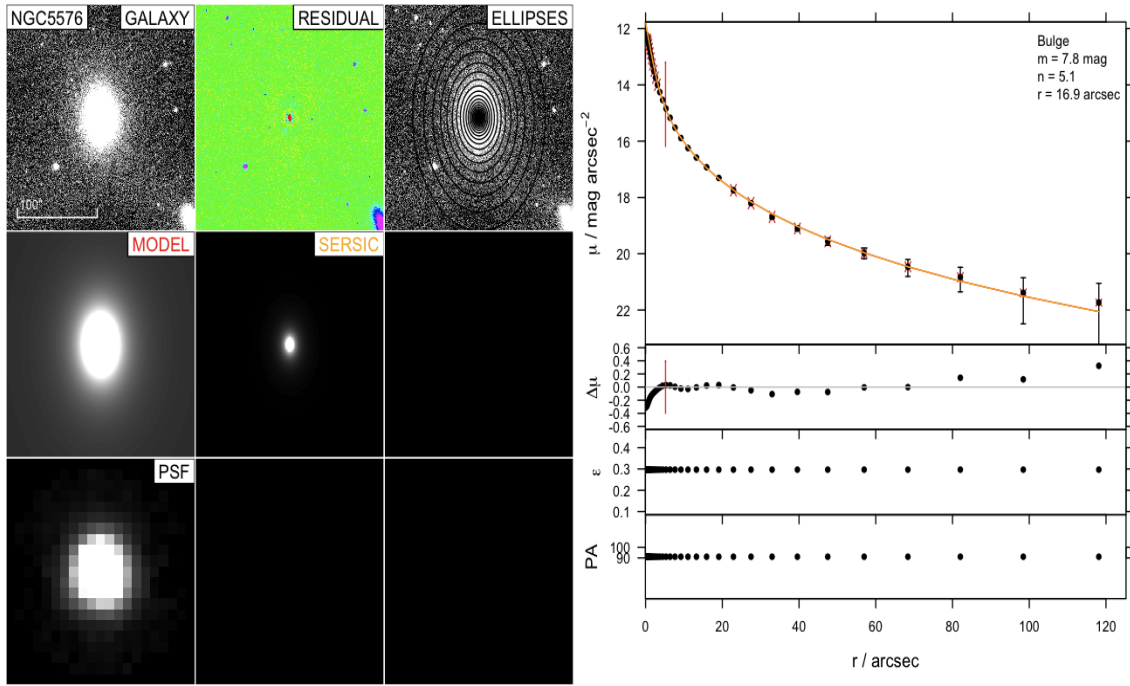


Figure 28. The surface brightness profile for NGC5576, we masked the inner 5.2 arcsec. The layout is as in Figure 5.

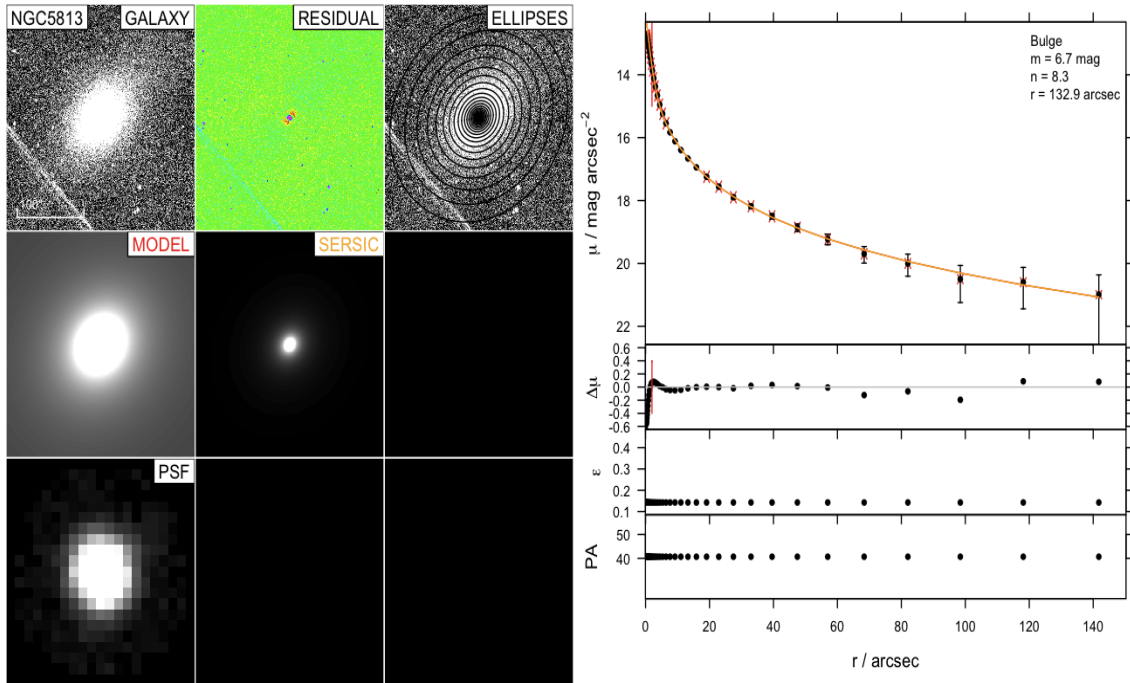


Figure 29. The surface brightness profile for NGC5813, we masked the inner 2 arcsec. The layout is as in Figure 5.

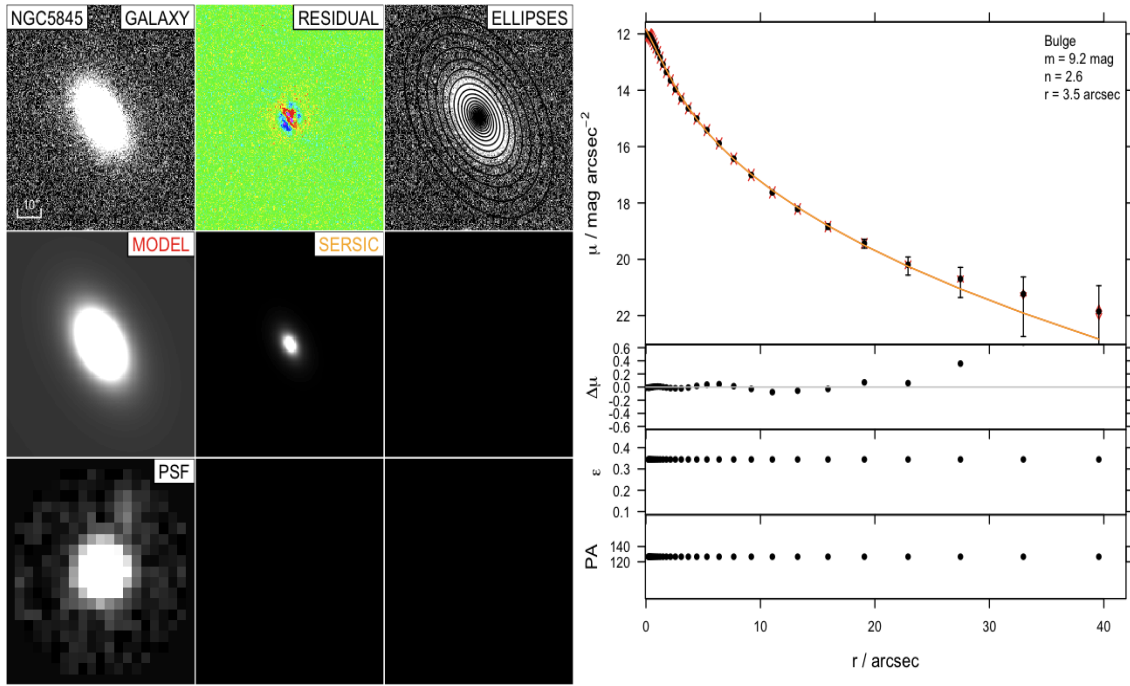


Figure 30. The surface brightness profile for NGC5845. The layout is as in Figure 5.

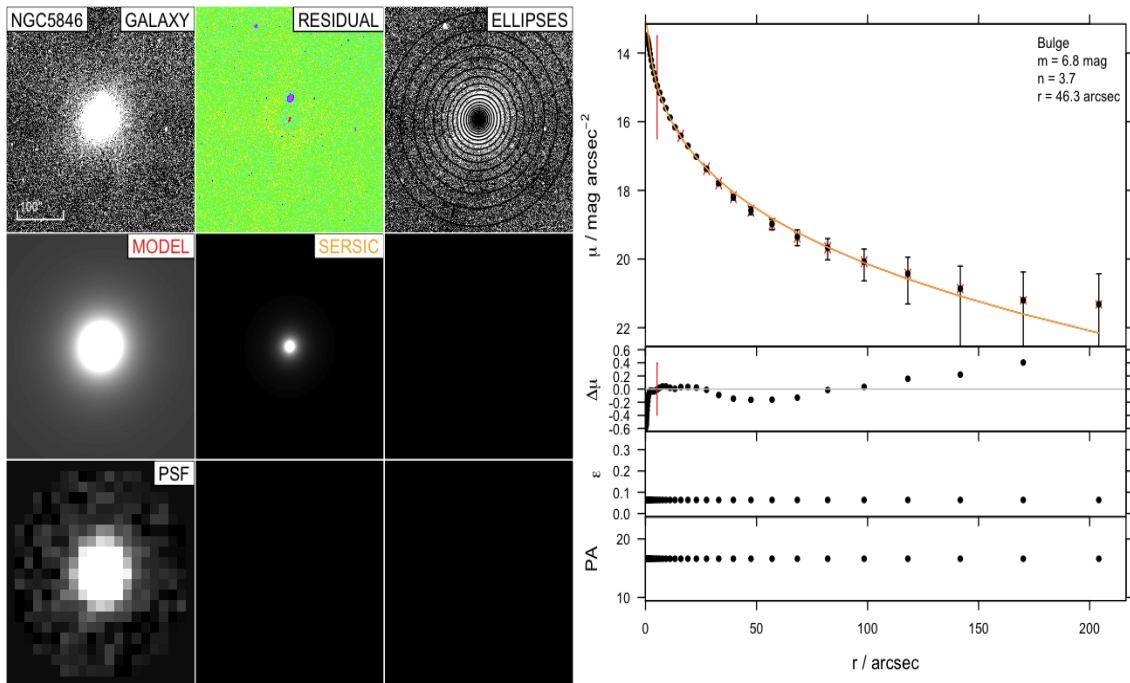


Figure 31. The surface brightness profile for NGC5846, we masked the inner 5.2 arcsec. The layout is as in Figure 5.

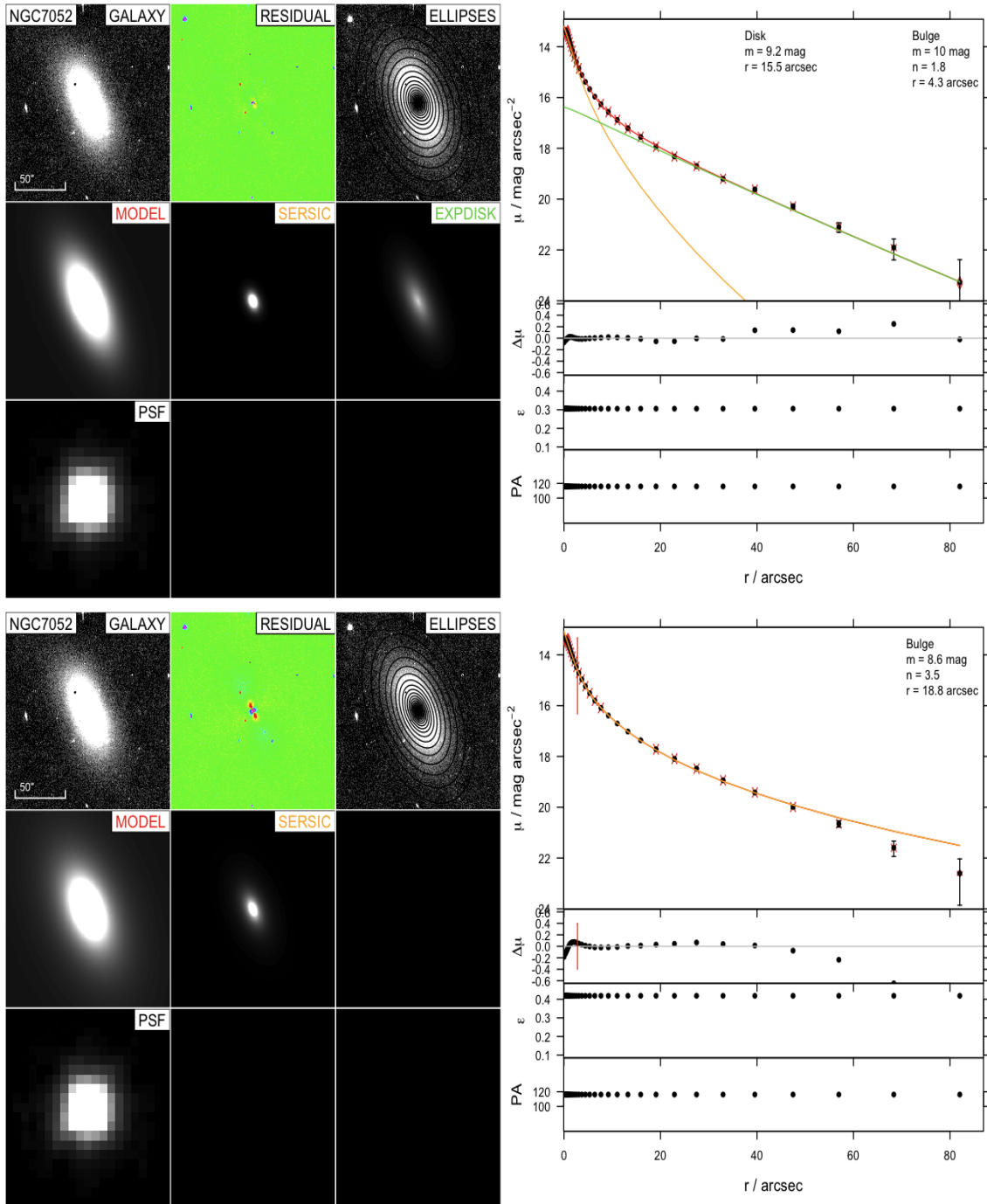


Figure 32. Previous studies model NGC7052 with a single Sérsic model. We found the galaxy can be profiled accurate by adding an additional component. The layout is as in Figure 5.

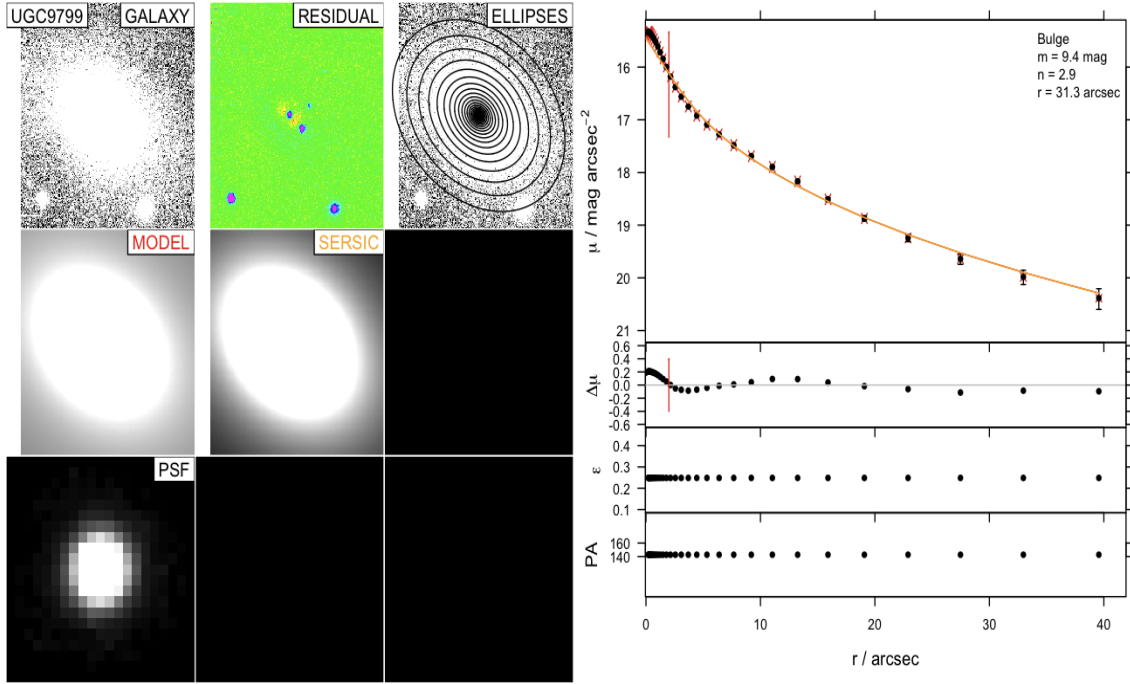


Figure 33. The surface brightness profile for UGC9799, we masked the inner 2 arcsec. The galaxy is placed at the edge of the image that makes difficult to constrain the fit. The layout is as in Figure 5.

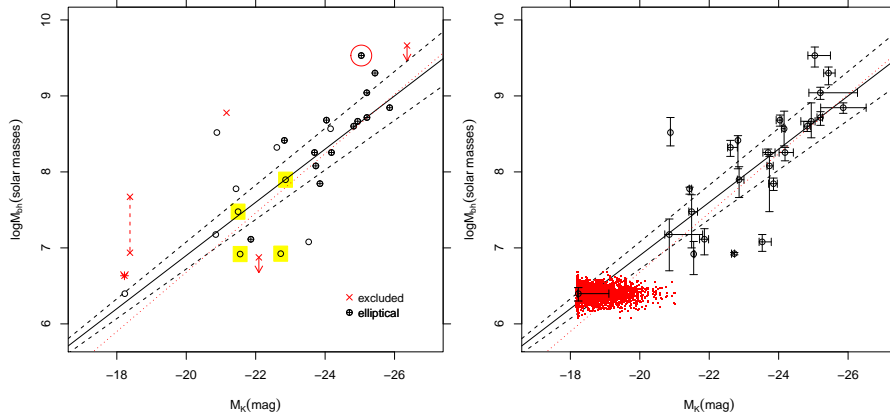


Figure 34. Left panel: The $M_{\text{bh}}-L_K$ relation for the full sample (solid line) with 1σ uncertainty (dashed line). The circles with a cross indicate elliptical galaxies. The yellow rectangular symbol denote galaxies with bar. The red dotted line comes from Graham et al. (2007, eq.13). The four galaxies excluded for the fitting (red crosses) are NGC863, NGC4435, UGC9799 and NGC4486B. The red star indicate the position of the Milky Way which has not been included in the line fit but shown merely for reference. The red dashed line connects the two possible black hole masses for the galaxy NGC863. The red circle indicate the galaxy NGC4486. Right Panel: Same plot as the left panel with the addition of the individual error bars. See §4.3 for details.

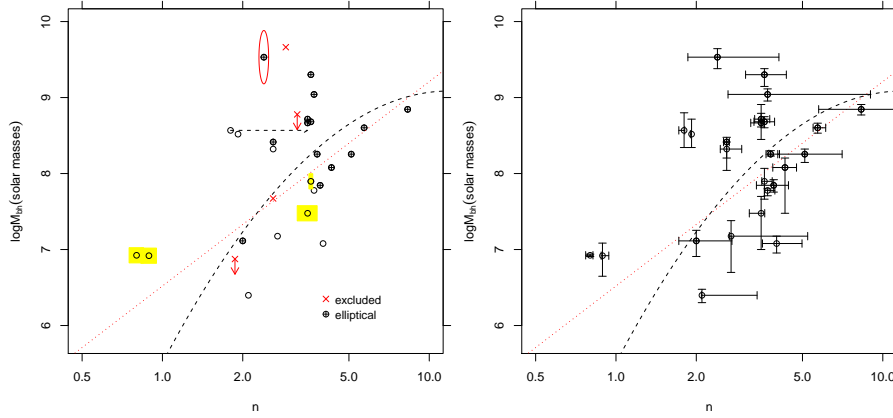


Figure 35. The SMBH mass versus the spheroid Sérsic index in the K-band. Different groups of galaxies are indicated with different symbols as in Figure 34. The black dashed line indicate the Sérsic index of NGC7052 for a single Sérsic fit. The linear and quadratic $M_{\text{bh}}-n$ relation of GD07 are shown as a red dotted line and a black dashed curve.

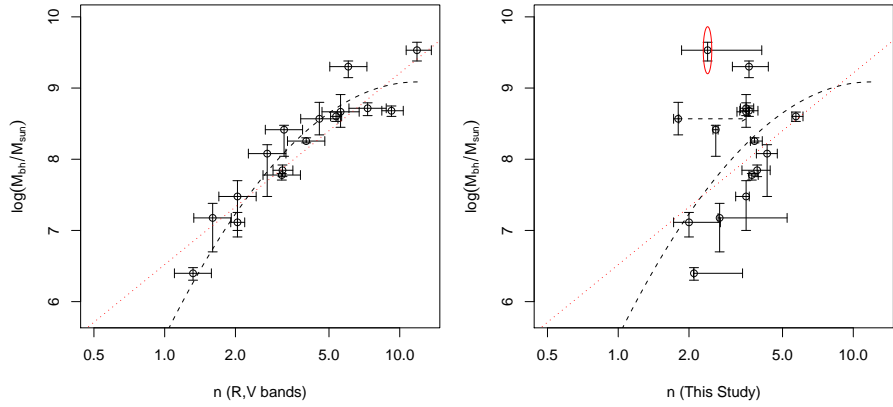


Figure 36. Comparison between this study Sérsic index and values from literature. Left panel: Correlations between supermassive black hole mass and the Sérsic index of the spheroid for a subset of my sample reported from **1D** fitting in R,V bands by Graham & Driver (2007); Kormendy et al. (2009); Seigar et al. (2007). Dotted and dashed lines are GD07 best linear and quadratic fits. Right panel: The same galaxies as left panel but with the Sérsic indices derived from this study with **2D** fit.